Journal of Hazardous Materials 441 (2023) 129882

Contents lists available at ScienceDirect

Journal of Hazardous Materials

journal homepage: www.elsevier.com/locate/jhazmat

Tunning active oxygen species for boosting Hg^0 removal and SO_2-resistance of Mn-Fe oxides supported on $(NH_4)_2S_2O_8$ doping activated coke

Xueyu Du [a,b], Caiting Li [a,b,*], Jie Zhang [a,b], Youcai Zhu [a,b], Caixia Liang [a,b], Le Huang [a,b], Kuang Yang [a,b], Chaoliang Yao [c], Ying Ma [c]

[a] College of Environmental Science and Engineering, Hunan University, Changsha 410082, PR China
[b] Key Laboratory of Environmental Biology and Pollution Control (Hunan University), Ministry of Education, Changsha 410082, PR China
[c] Yonker Environmental Protection Co., Ltd, Changsha 410330, PR China

HIGHLIGHTS

- $(NH_4)_2S_2O_8$ modified AC loaded with MnO_x-FeO_x was used for Hg^0 removal.
- The priority of active oxygen species for Hg^0 removal was as C=O > COO- > O_L.
- FeO_x enhanced SO_2-resistance via weakening its adsorption on C=O and COO-.
- The motivation of O_2 mainly accounted for the regeneration of lattice oxygen species.

GRAPHICAL ABSTRACT

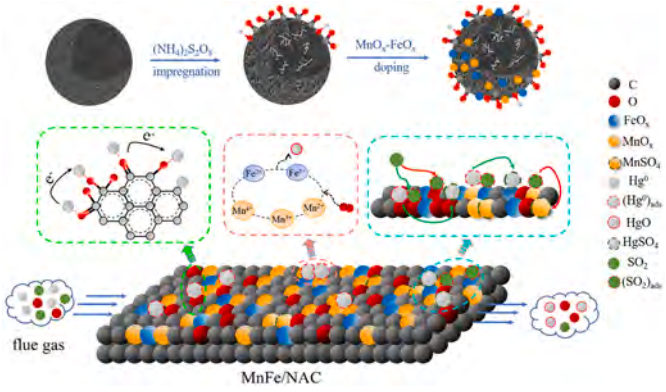

ARTICLE INFO

Editor: Haizhou Liu

Keywords:
MnFe/NAC
oxygen functional groups
Hg^0 control
SO_2-resistance
Hg-TPD

ABSTRACT

Active oxygen species (AOS) play an essential role in modulating the activity of activated coke (AC) based samples. In this paper, AC was endowed with abundant AOS by modifying with $(NH_4)_2S_2O_8$ and MnO_x-FeO_x for Hg^0 removal. $(NH_4)_2S_2O_8$ treatment induced abundant micropores and oxygen-containing functional groups, and thus provided more anchoring sites for the dispersion of MnO_x-FeO_x. The synergy of MnO_x-FeO_x and interaction between MnO_x-FeO_x and NAC support contributed to a larger surface area, highly-dispersed active components, stronger reducibility, and more metal ions with high valence of MnFe/NAC. The optimal MnFe/NAC exhibited superior Hg^0 removal efficiency above 90% at 120~180 ℃, as well as excellent performance for simultaneous removal of Hg^0 and NO, and 600 ppm SO_2 and 8 vol.% H_2O addition led to a slight deterioration. XPS and Hg-TPD revealed that mercury adsorbed on MnFe/NAC included phy-Hg, C=O-Hg, COO-Hg, and O_L-HgO. Besides, the priority of AOS for Hg^0 chemisorption was C=O > COO- > O_L, and Hg^{2+} was also detected in the outlet. Moreover, the SO_2-poisoning effect was ascribed to the sulfation of MnO_x and the occupation of COO- and C=O, and FeO_x incorporation enhanced the SO_2-resistance through weakening SO_2 adsorption on C=O and COO-. The motivation of O_2 mainly contributed to the regeneration of AOS, especially O_L. The excellent regeneration

* Corresponding author at: College of Environmental Science and Engineering, Hunan University, Changsha 410082, PR China.
E-mail address: ctli@hnu.edu.cn (C. Li).

https://doi.org/10.1016/j.jhazmat.2022.129882
Received 24 May 2022; Received in revised form 6 August 2022; Accepted 28 August 2022
Available online 31 August 2022

performance and stability further affirmed the application potential of MnFe/NAC for Hg^0 capture from coal-fired flue gas.

1. Introduction

As a naturally mineralized element in fossil flues, mercury has been regarded as one of the "ten leading chemicals of concern" by the World Health Organization due to its extreme toxicity, long-range migration, high volatility, and ability to bioaccumulate (Wang et al., 2020a; Kong et al., 2018; Yang et al., 2022b) Coal-fired power plants, with high coal consumption, are one of the largest anthropogenic mercury emission sources and account for almost 40% of the total mercury emission in China (Pirrone et al., 2010; Streets et al., 2017). To reduce the air pollution, Emission Standard for Air Pollutants for Thermal Power Plants (GB 13223-2011) has been issued for limiting the mercury emission to 0.03 mg/m^3 by the Ministry of Environmental Protection (MEP) of China (Emission Standard of Air Pollutants for Thermal Power Plants, 2011). Differing from oxidized mercury (Hg^{2+}) and particle-bound mercury (Hg^P), the intrinsic high-volatility and low-solubility prevent elemental mercury (Hg^0) from effective capture by wet flue gas desulfurization (WFGD) or particulate control devices (PCDs) (Chen et al., 2016). Therefore, numerous methods have been developed to control the Hg^0 emission from coal-fired flue gas (Yang et al., 2020a).

Among these technologies, adsorption has attracted more and more attentions owing to its simplicity and efficiency, and the selection of sorbents with high efficiency and cost-effectiveness is the core issue (Liu et al., 2018). Generally, carbon-based sorbents (Yang et al., 2022a), mineral-based sorbents (Ma et al., 2021), calcium-based sorbents (Yang et al., 2011), metal- and metal-oxide-based sorbents (Wang et al., 2020c; Yang et al., 2020b), metal-organic-framework-based sorbents (Dong et al., 2019) and fly ashes (Liu et al., 2020b) are commonly used for Hg^0 removal. Hereinto, activated coke (AC), as one product of lignite, not only possesses a well-developed porous structure and abundant oxygen functional groups comparable to activated carbon, but also exhibits greater mechanical strength, better adsorption kinetics beneficial to high utilization of surface, superior regeneration performance and lower cost than activated carbon (Du et al., 2021; Liu et al., 2019c; Zhang et al., 2022). Consequently, AC is regarded as a potential candidate of activated carbon for Hg^0 removal with its range of sources, abundance, and low cost. However, on account of its limited surface active sites, the adsorptive capacity of raw activated coke is still unsatisfactory for Hg^0 removal. Therefore, how to optimize the active oxygen species and porous structure of AC has become a hotspot of research.

Various transitional metal oxides, such as MnO_x (Liu et al., 2019a), CuO (Li et al., 2020), CeO_2 (Fan et al., 2010), CoO_x (Zhang et al., 2019), FeO_x (Tan et al., 2012), and the binary metal oxides (Zhou et al., 2020; Yang et al., 2019; Chen et al., 2018) have been widely explored as active components to optimize active oxygen species of carbon-based materials for Hg^0 removal. Thereinto, manganese oxides received remarkable attentions for its high structure flexibility and superior oxidative activity at low temperatures (Xu et al., 2017). Liu et al. fabricated a MnO_2 nanoparticle-doped carbon nitride nanosheet (CNNS), and $10MnO_2$/CNNS presented the Hg^0 removal efficiency above 91% within a wide temperature range of 90~240 ℃, in which the enhanced electron transfer at the interface of MnO_2 and g-C_3N_4 and the lattice oxygen provided by the redox couple of Mn^{4+}/Mn^{3+} worked (Liu et al., 2019a). Zhou et al. found the partial oxidation reaction between $KMnO_4$ and starch-bentonite (BS) led to the introduction of carbonyl and ester groups, which benefited for the enhanced Hg^0 removal (Zhou et al., 2019). However, MnO_x/BS exhibited a poor tolerance to SO_2 and H_2O, and the decline of ~29% Hg^0 capture efficiency was detected with the addition of 800 ppm SO_2 and 10 vol.% water vapor. FeO_x doping was reported to decrease the rate of sulfate formation and thus strengthen the SO_2-resistance of Mn-Ce/TiO_2 to a large extent (Shen et al., 2010). Besides, Kang et al. demonstrated that the incorporation of FeO_x was an effective strategy to improve SO_2 tolerance via suppressing SO_2 adsorption on $CeVO_4$ catalysts (Kang et al., 2020). Moreover, the intrinsic magnetism of iron oxides realized the effective separation of sorbents from fly ash by an external magnetic field to ensure the recycle of fly ash, and the separated sorbents could be recovered for further Hg^0 removal (Yang et al., 2016; Xin et al., 2022). Above all, MnO_x-FeO_x was chosen as the active components to endow AC with abundant active oxygen species for effective removal of Hg^0. However, metal oxides with a higher loading desirable for excellent activity were prone to agglomeration when synthesized, which inhibited the sufficient release of the catalytic potential of MnO_x-FeO_x (Ma et al., 2020).

In order to restrain the agglomeration, oxidative acid treated AC was adopted to facilitate the dispersion of active components. Xue et al. modified AC with HNO_3, H_2SO_4, and H_2O_2 as support for subsequent loading of CuO, respectively. The characterization results showed the pretreatment improved the specific surface area and the amount of surface oxygen-containing groups, thus providing more anchoring sites for CuO nanoparticles (Xue et al., 2008). However, there were few studies concerning AC treated with $(NH_4)_2S_2O_8$, as a strong oxidant with low cost, served as support of MnO_x-FeO_x for Hg^0 removal, and how $(NH_4)_2S_2O_8$ affects the physicochemical properties is still not clear.

In this work, we synthesized MnO_x-FeO_x supported on $(NH_4)_2S_2O_8$ modifying AC for enhanced Hg^0 removal, and explored how active oxygen species worked in Hg^0 removal under different operation conditions. Hg-temperature-programmed desorption was conducted, in which mercury species bonded with the sample in different forms would be desorbed at different temperatures (Liu et al., 2019c). And three aspects are mainly focused on: (i) Hg^0 removal, SO_2-resistance and regeneration performance of modified AC samples; (ii) the role of active oxygen species during Hg^0 removal via Hg-temperature-programmed desorption; (iii) the mechanism relevant to Hg^0 removal and SO_2 tolerance proposed with the aid of experiment, kinetic analysis and characterization. The objective of the work is to provide a first-time insight into the properties-activity relationship of MnFe/NAC, and exploit a cost-effective and promising sorbent for eliminating Hg^0 from coal-fired flue gas.

2. Experimental section

2.1. Sample synthesis

The $(NH_4)_2S_2O_8$-modified activated coke (denoted as NAC) was prepared by impregnation method. Firstly, the columnar AC (Alxa League Ke'xing Carbon Industry) was crushed into particles (20-40 mesh). To remove the impurity on the surface or in the pores, AC particles were washed with deionized water under ultrasonic repeatedly and then dried overnight. For NAC, the particle AC was immersed in 1 mol/L $(NH_4)_2S_2O_8$ solution for 24 h, and then washed to pH > 5. After dried at 50 ℃ for 4 h and 105 ℃ for another 10 h, the sample was calcined at 400 ℃ for 2 h with N_2.

MnO_x and/or FeO_x were loaded on NAC by impregnating NAC into the aqueous solution containing the appropriate amount of 50 wt.% Mn $(NO_3)_2$ solution and $Fe(NO_3)_3 \bullet 9H_2O$ for 24 h. According to our previous study, the molar ratio of Mn/Fe was designed as 3:1, and the loading of transitional metal was set as 6 wt% to the mass of modified samples, which endowed the sample possessed well-developed porous structure, abundant active oxygen species and more metal atoms with higher valence (Du et al., 2018). Then the precursor was placed at 105 ℃ for 12 h and calcined at 500 ℃ for 4 h under N_2. The obtained sample was

labeled as MnFe/NAC. For comparison, MnFe/AC was prepared in the similar method.

2.2. Experimental setup

The Hg^0 removal was conducted on the fix-bed quartz reactor (i.d. = 10 mm, L = 600 mm) to evaluate the activity of prepared samples, as depicted in Fig. S1 (Liu et al., 2019c). It should be noticed that the relatively high Hg^0 concentration and space velocity was employed to reduce the experimental errors caused by the sensitivity of the mercury analyzer and to allow experiments to be completed in a reasonable time scale. Typically, 0.15 g sample was loaded in the middle of quartz reactor, in which the temperature was controlled with the thermocouple at 60~180 ℃, and 0.10 g sample was used to investigate the effect of SO_2, H_2O and HCl. The simulated flue gas controlled by mass flow meter was composed of 120 μg/m^3 Hg^0, 0-600 ppm SO_2, 0-400 ppm NO, 0-400 ppm NH_3, 0-10 ppm HCl, 0-6% O_2, 0-8 vol.% H_2O and N_2 as balanced gas, which was maintained at the gas hourly space velocity (GHSV) of ~190,000 h^{-1}. Thereinto, the feed of gaseous Hg^0 was generated by flowing 100 mL/min N_2 through a Hg^0 permeation tube (VICI Metronics, USA) that was placed in the temperature-controlled water bath. The concentration of inlet Hg^0 and outlet Hg^0 was monitored continuously by an on-line RA-915M mercury analyzer (LUMEX Ltd, Russia). To identify the amount of Hg^0 oxidation over samples, the mercury speciation conversion system, consisting of the impingers with 10% NaOH solution and 10% $SnCl_2$ solution, was applied to convert Hg^{2+} into Hg^0. To be specific, NaOH solution was used to remove SO_2 from flue gas, and then Hg^{2+} was reduced with the aid of $SnCl_2$. Moreover, the blank experiment indicated that no obvious Hg^0 removal was detected in the absence of samples. The outlet Hg^0 concentration was measured at a steady-state condition after the reaction was prolonged for 2 h. As an effective method to explore the mercury species adsorbed on samples during Hg^0 removal, the temperature-programmed desorption of Hg (Hg-TPD) was then conducted for the treated sample in 500 mL/min N_2 with a heating rate of 5 ℃/min. Thereinto, to probe into the priority of active oxygen species in Hg^0 removal with the aid of Hg-TPD, the sample was firstly pretreated with simulated flue gas for 1, 2 and 4 hours.

The removal efficiency (E_T), adsorption efficiency (E_{ads}) and oxidation efficiency (E_{oxi}) of Hg^0 was defined as follows:

$$E_T = \frac{Hg^0_{in} - Hg^0_{out}}{Hg^0_{in}} \times 100\% \quad (1)$$

$$E_{ads} = \frac{Hg^0_{in} - Hg^T_{out}}{Hg^0_{in}} \times 100\% \quad (2)$$

$$E_{oxi} = \frac{Hg^T_{out} - Hg^0_{out}}{Hg^0_{in}} \times 100\% \quad (3)$$

in which Hg^0_{in} and Hg^0_{out} indicate the Hg^0 concentration in the inlet and outlet flue gas, respectively, and the Hg^T_{out} is the Hg^0 concentration in the outlet flue gas that passed through the mercury speciation conversion system.

The NO conversion efficiency (E_{NO}) was calculated as:

$$E_{NO} = \frac{NO_{in} - NO_{out}}{NO_{in}} \times 100\% \quad (4)$$

where NO_{in} and NO_{out} represented the NO concentration (ppm) in the inlet and outlet.

The q is described as the amount of Hg^0 adsorbed on per gram of activated coke when the sample reached breakthrough, which is calculated as follows:

$$q = \frac{F}{m}\int_0^t \left(Hg^0_{in} - Hg^0_{out}\right) d_t \quad (5)$$

where F is the total flow rate (m^3/min), m denotes the mass of sample used for the Hg^0 breakthrough experiment (g), and t is the breakthrough time (min).

Besides, to elucidate the specific the removal mechanism and determine rate-controlling step, the pseudo-first-order kinetic model, pseudo-second-order kinetic model, intraparticle diffusion model and Elovich model were applied to fit the dynamic adsorption process of Hg^0 which are expressed as Eqs. 6–9 (Wu et al., 2009; Simonin, 2016; Diagboya et al., 2015):

$$\frac{d_{q_t}}{d_t} = k_1\left(q_e - q_t\right) \quad (6)$$

$$\frac{d_{q_t}}{d_t} = k_2\left(q_e - q_t\right) \quad (7)$$

$$q = k_{id}t^{1/2} + C \quad (8)$$

$$q = (1/\beta)\ln(t + 1/\alpha\beta) - (1/\beta)\ln(1/\alpha\beta) \quad (9)$$

where q_t (μg/g) and q_e (μg/g) are Hg^0 adsorption capacities of sample at time t and equilibrium, respectively; k_1 (s^{-1}), k_2 (μg/(g•s)) and k_{id} (μg/(g•$s^{1/2}$)) are the pseudo-first-order rate constant, the pseudo-second-order rate constant and the intraparticle diffusion rate constant, respectively; t is the adsorption time (s), and C is the constant relevant to the thickness of the boundary layer (μg/g); α is the initial adsorption rate (μg/(g•$s^{1/2}$)), and β is a constant relevant to the surface coverage and activation energy (μg/g).

2.3. Sample characterization

The porous structural characteristics of samples were determined by N_2 adsorption-desorption on an ASAP 2460 analyzer (USA, Micromeritics) after the degasification at 180 ℃ for 10 h. The morphology images were collected by a scanning electron microscope (Zeiss Sigma 300, Germany). The X-ray diffraction (XRD) patterns were acquired on a Rigaku rotaflex D/Max2500 using a Cu-Kα radiation source (45 KV, 40 mA) in the range of 2θ=10-80 ° with a scanning rate of 5 °/min. The ultimate analysis of AC and NAC were conducted using the Elementar Analysensystem GmbH vario (Elementar Ltd Corp, Germany). The surface chemistry of the elements on the sample was analyzed by X-ray photoelectron spectroscopy (XPS) with the Al Kα radiation (Escalab Xi+, USA), and C 1 s at 284.80 eV was measured as the reference to calibrate the binding energy of obtained spectra. H_2-temperature-programmed reduction (H_2-TPR) and O_2-temperature-programmed desorption (O_2-TPD) were performed at the TP-5080 automatic chemical adsorption instrument (Tianjin Xian Quan, China). Prior to the measurement, the sample was first placed into 30 mL/min He and heated to 200 ℃ at a heating rate of 10 ℃/min. After being pretreated for 1 h, the sample was cooled down to 50 ℃. For O_2-TPD, the sample was exposed to 30 mL/min 5% O_2/He for 1 h to adsorb O_2, thereafter purged by He. Finally, the sample was heated to 600 ℃ with a ramp of 10 ℃/min. In the case of H_2-TPR, the sample was purged under the atmosphere of 10% H_2/Ar for 1 h. And TCD signals were collected by measuring H_2 consumption from 50 to 850 ℃ with a heating rate of 10 ℃/min. As an effective method to analyze the oxygen functional groups, the Fourier Transform Infrared Spectroscopy (FT-TR) was collected in range of 400-4000 cm^{-1} on a Thermo Scientific Nicolet iS10. Both fresh MnFe/NAC and MnFe/NAC treated with 500 mL 120 μg/m^3 Hg^0 +6% O_2/N_2 gas flow at 120 ℃ for 2 h were analyzed to explore the change of oxygen functional groups during Hg^0 removal. Prior to each measurement, the sample was heated at 180 ℃ in pure N_2 for 2 h so as to remove the moisture adsorbed on samples.

3. Results and discussion

3.1. Structural, morphology and textural properties

The N_2 adsorption-desorption isotherms of prepared samples were shown in Fig.1(a). According to the Brunauer-Deming-Deming-Teller (BDDT) classification, both AC and modified AC were of type I isotherm with type H4 hysteresis loop, indicating the majority of nitrogen uptake occurred in micropores. And the microporous structure explained the unclosed curves at low pressure ($P/P_0 < 0.12$). As the relative pressure increased, the N_2 adsorption reached a plateau due to the appearance of multilayer adsorption on samples (Liu et al., 2020a). For Fe/NAC and MnFe/NAC, an increased nitrogen uptake at higher relative pressure ($0.9<p/p_0<1$) suggested a higher portion of nitrogen adsorption in macropores. Besides, as depicted in Fig. 1(b), all samples presented the narrow pore size distribution at 0.5~2 nm, implying the uniform microporous structures. Two peaks at 0.733 and 1.591 nm were observed for virgin AC, and the modification with $(NH_4)_2S_2O_8$ and/or MnO_x-FeO_x led to the peaks shifting to lower pore diameter, especially for Fe/NAC and MnFe/NAC. Consequently, the higher portion of micropores contributed to an enhanced S_{micro} and V_{micro}, as well as a decreased D_p for modified AC samples, and thus a marked growth in S_{BET} and V_p (Table 1). Besides, a general positive correlation was observed between fractal dimension (D_s) and generation of micropores, which means a higher space filling ability and more adsorption sites (Avnir et al., 1983). It was noticed that although with a stronger peak at a lower pore diameter, Fe/NAC and MnFe/NAC possessed larger D_p when compared with other modified ACs. And the formation of mesopores and macropores on Fe/NAC and MnFe/NAC depicted in the insert of Fig. 1 (b) should be responsible for it. For all samples, Fe/NAC possesses the highest specific surface area and the largest pore volume for both micropores and total pores, as well as the highest pore diameter. In general, the pickling with acid $(NH_4)_2S_2O_8$ solution facilitated the generation of more micropores in AC (Zhao et al., 2019). And during the following calcination, MnO_x and FeO_x promoted the deep catalytic cracking, dehydrogenation of macromolecules and the release of volatiles, which prevented the blockage and benefited for the developed porous structure (Shen et al., 2014).

As shown in Fig. 2, the changes on morphology after modification with $(NH_4)_2S_2O_8$ and metal oxides were explored. It was obvious that the impregnation of $(NH_4)_2S_2O_8$ solution facilitated the generation of pores, and thus contributed to the higher surface area of NAC. Massive bulks were found over MnFe/AC, demonstrating the poor dispersion of MnO_x-FeO_x on AC support. MnO_x presented as irregular cubes along with some agglomeration over the surface of Mn/NAC, while smaller particles and lower agglomeration were detected for Fe/NAC. Besides, the incorporation of FeO_x into Mn/NAC further accelerated the dispersion of metal oxides with smaller particles.

XRD characterization was performed to detect the crystal phase structure of virgin AC and modified AC, as depicted in Fig. 3. The characteristic peaks attributed to SiO_2 (2θ=19.742°, 29.188° and 35.427°, PDF 40-1498) and C (2θ=26.603°, 43.015°, PDF 26-1080) were detected for virgin AC. Although with some changes, the peaks at 19.742° and 26.603° of virgin AC were still retained after modification. Loading with MnO_x-FeO_x, Fe_3O_4 (2θ=55.544°, PDF 26-1136) and MnO_2 (2θ=62.707° and 65.089°, PDF 42-1316) crystalline phase were formed in MnFe/AC. The modification of MnO_x on NAC induced the appearance of peaks at 32.411°, 36.040°, 44.369°, 58.763° and 60.024°, which corresponded to Mn_3O_4 (PDF 18-0803). With respect to Fe/NAC, the peaks relative to Fe_2O_3 (2θ=35.709°, 43.132° and 59.914°) were observed. Besides, the crystalline size calculated by the Scherrer equation and MDI Jade software was 24.336, 36.248 and 17.191 nm for MnFe/AC, Mn/NAC and Fe/NAC, respectively. In accordance with SEM results, no peaks were observed over MnFe/NAC, revealing MnO_x-FeO_x were well-dispersed or in the form of amorphous states. Two aspects should be responsible for it. The higher surface area after $(NH_4)_2S_2O_8$ modification provided more anchoring sites for the dispersion of MnO_x-FeO_x. Besides, the synergy effect between MnO_x-FeO_x further improved the dispersion of active components.

3.2. Surface chemical properties

3.2.1. XPS analysis

With $(NH_4)_2S_2O_8$ impregnation, an increase of 0.18% and 0.08% were observed for O and S, while the content of C and N were reduced by 0.21% and 0.06%, respectively (Table S1). It indicated $(NH_4)_2S_2O_8$ introduced more active oxygen and sulfur species in activated coke (Wang et al., 2016). To further probe into the change of the chemical state of elements, XPS was carried out.

As depicted in Fig. 4(a), C 1 s spectra could be resolved into four peaks, which were attributed to graphic C (C=C) at ~284.80 eV, alcohol or ether groups (COR) at ~286.30 eV, carbonyl groups (C=O) at ~287.62 eV and carboxyl or ester groups (COOR) at 289.30±0.05 eV, respectively (Shen et al., 2008). Obviously, the generation of more C=O and COOR after $(NH_4)_2S_2O_8$ oxidation was observed. High-resolution O 1 s spectra featured peaks at ~531.80 eV, ~532.70 eV, 533.5-533.8 eV and ~534.60 eV, relevant to carbonyl (C=O), alcohol or ether groups (COR), ester groups (COO-) and adsorbed water and oxygen (O_{ads}), respectively (Zhou et al., 2007). In agreement with C 1 s, an increase of 10.36% and 13.59% was found for carbonyl and ester groups on account of modification with $(NH_4)_2S_2O_8$, respectively (Table 2). Besides, an increased O_{ads} indicated the formation of active sites for the adsorption of reactant gases with the aid of developed micropore structure (Yan et al., 2013). In terms of sulfur, the characteristic peaks of S^{2-} (164.01

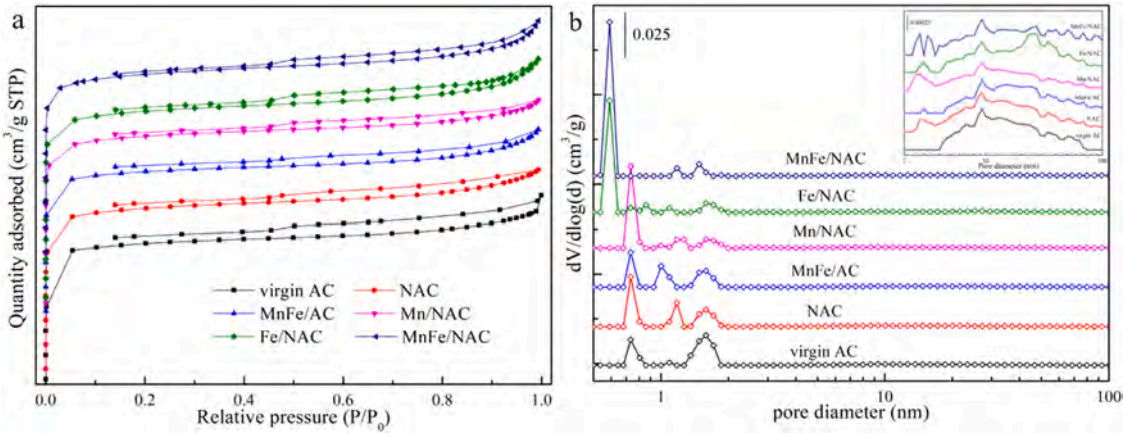

Fig. 1. (a) N_2 adsorption-desorption isotherms and (b) pore size distributions of prepared samples.

Table 1
BET surface and pore parameters of the prepared samples.

Samples	S_{BET} (m^2/g)	S_{micro} (m^2/g)	S_{micro}/S_{BET}	V_p (cm^3/g)	V_{micro} (cm^3/g)	V_{micro}/V_p	D_p (nm)	[a]D_s	[b]Cry (nm)
Virgin AC	260.212	226.955	0.872	0.154	0.087	0.565	2.372	2.494	-
NAC	298.873	261.627	0.875	0.142	0.101	0.711	1.895	2.705	-
MnFe/AC	263.718	230.703	0.875	0.130	0.089	0.685	1.976	2.672	24.336
Mn/NAC	308.006	270.834	0.879	0.144	0.105	0.729	1.869	2.862	36.248
Fe/NAC	331.529	308.601	0.931	0.164	0.121	0.738	1.973	2.765	17.191
MnFe/NAC	321.670	296.722	0.922	0.162	0.117	0.722	2.008	2.881	-

[a]: the fractal dimension of samples calculated by Frenkl-Halsey-Hill equation based on N_2 adsorption isotherm, in which a linear correlation was found between ln(V) and ln(ln(p/p_0)). And the slope was regarded as D_s of samples.
[b]: the crystalline of samples.

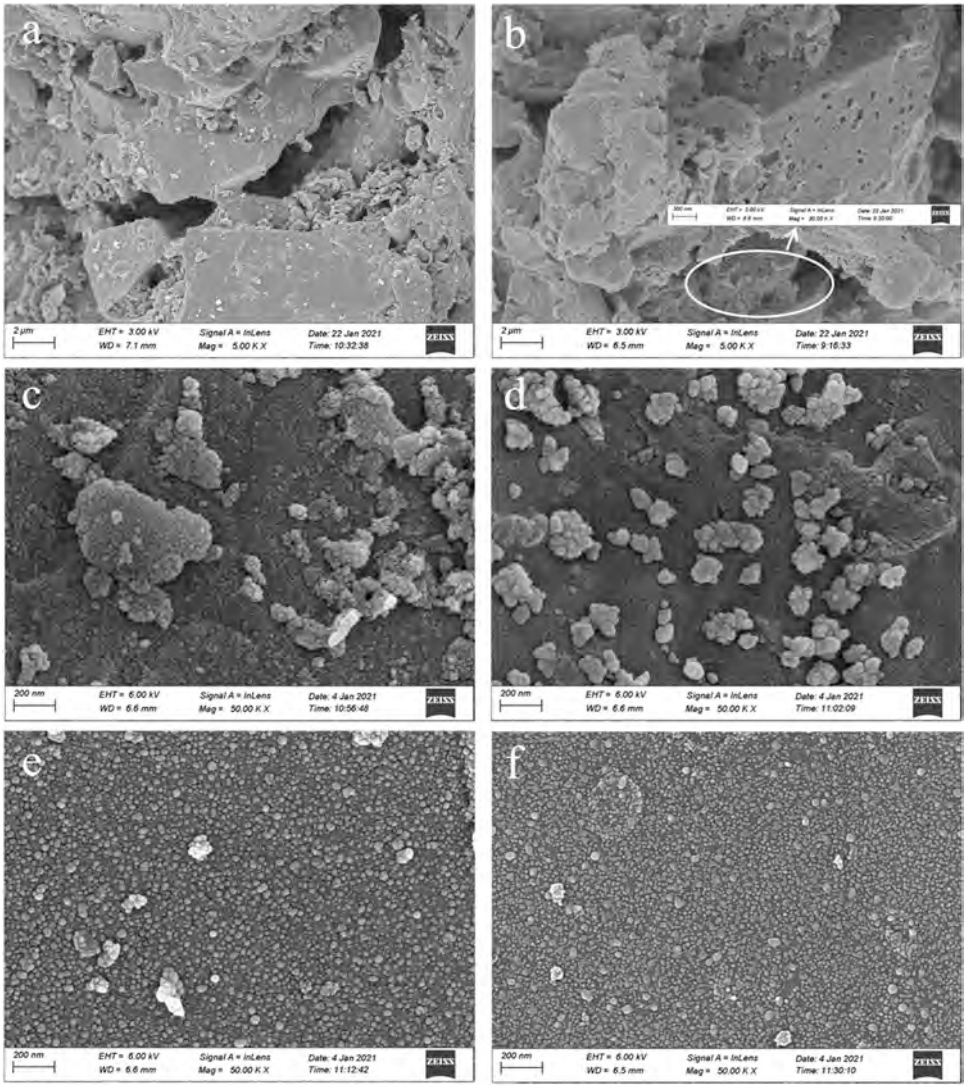

Fig. 2. SEM images of (a) virgin AC, (b) NAC, (c) MnFe/AC, (d) Mn/NAC, (e) Fe/NAC and (f) MnFe/NAC.

±0.01 eV), S_2^{2-} (165.17±0.04 eV) and S^{6+} (169.05±0.05 eV) were detected for both AC and NAC (Hong et al., 2020). As shown in Table 2, In comparison with AC, S atoms with negative charge were transformed into SO_4^{2-} over NAC.

The XPS spectra of metal oxides doped samples were presented in Fig. 5. With the loading of metal oxides, a new peak at 530.30-530.40 eV appeared for the O 1 s spectra, which was reported as O_L (Ma et al., 2020). As summarized in Table 3, irrespective of the support, the co-dopant of MnO_x and FeO_x endowed samples with fewer lattice oxygen and more oxygen functional groups, especially for MnFe/NAC. Besides, with a higher specific surface area, MnFe/NAC possessed more O_{ads} than MnFe/AC. For Mn species, Mn $2p_{3/2}$ spectra were divided into three peaks centered at 641.10±0.10 eV, 642.40±0.10 eV and 644.2-644.6 eV, which were corresponded to Mn^{2+}, Mn^{3+} and Mn^{4+}, respectively (Yang et al., 2019; Liu et al., 2019b). The samples with NAC support possessed more Mn atoms in higher valence than that supported on virgin AC, which might be on account of the introduction of active oxygen species accompanied with $(NH_4)_2S_2O_8$ modification. Moreover, the cooperation of FeO_x into Mn/NAC contributed to a higher $Mn^{4+}/(Mn^{3+}+Mn^{2+})$ molar ratio, which further testified the strong

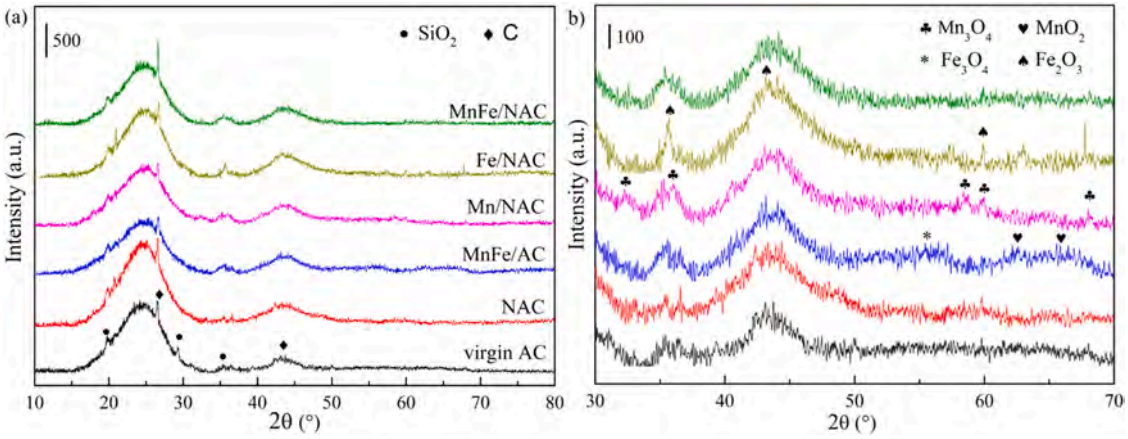

Fig. 3. XRD patterns at (a) 2θ=10-80°and (b) 2θ=30-70°of prepared samples.

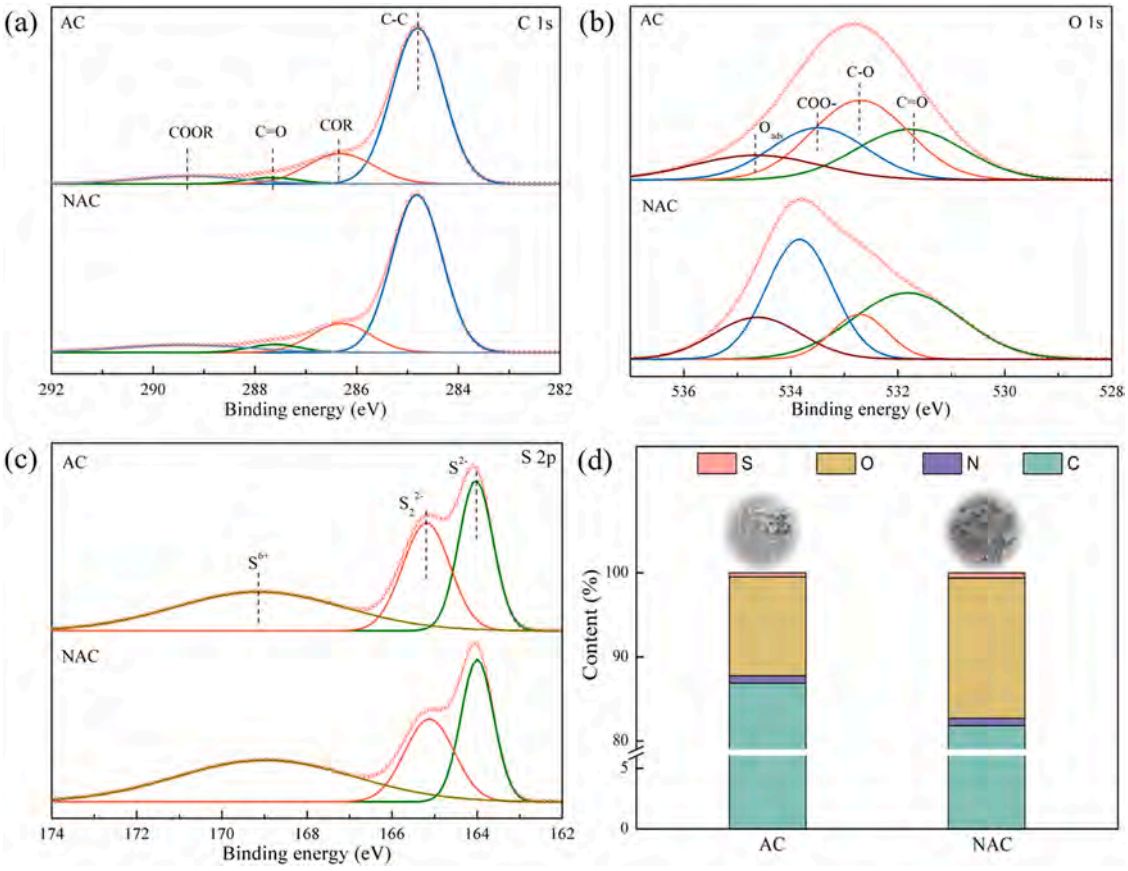

Fig. 4. XPS spectra of (a) C 1 s, (b) O 1 s and (c) S 2p and (d) atomic contents measured by XPS for AC and NAC.

Table 2
XPS relative intensity of prepared samples.

Relative intensity(%)	C 1 s				O 1 s				S 2p		
	C-C	COR	C=O	COOR	C=O	C-O	COO-	O_{ads}	S^{2-}	S_2^{2-}	S^{6+}
AC	72.81	16.63	2.97	7.59	25.70	36.32	23.59	14.39	28.17	32.32	39.15
NAC	71.83	15.55	3.75	8.87	36.06	11.71	37.18	17.05	37.01	19.06	43.93

synergy between MnO_x and FeO_x. And as shown in Fig. 5(b), the stronger intensity of peaks ascribed to Fe^{3+} at ~711.66 eV and 713.60-713.90 eV over MnFe/NAC also identified the synergistic effect between metal oxides (Jampaiah et al., 2019).

3.2.2. O_2-TPD

O_2-TPD was carried out to probe into the active oxygen species of the prepared samples. In general, the desorption peak at lower temperature indicated there existed weaker interaction forces between oxygen and

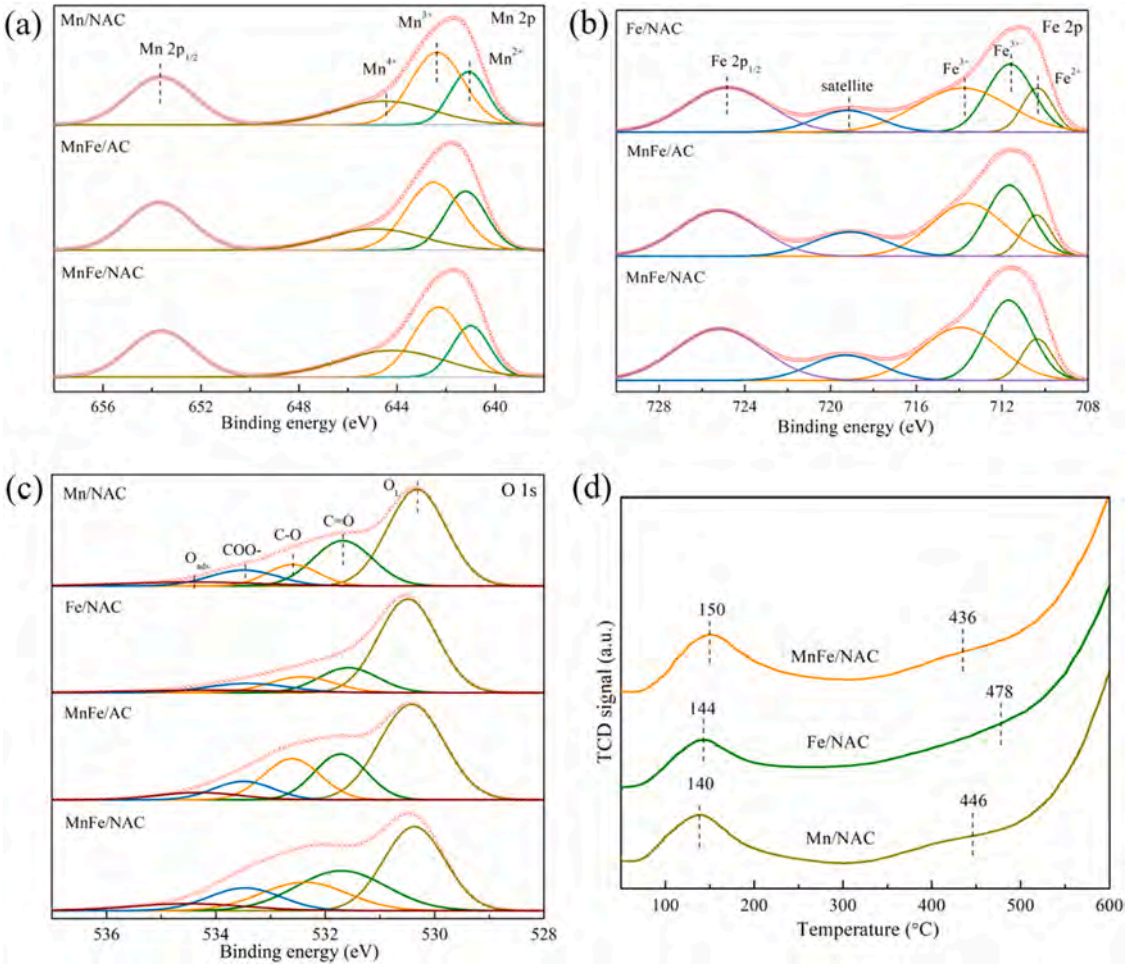

Fig. 5. XPS spectra of (a) Mn 2p, (b) Fe 2p, (c) O 1s and (d) O_2-TPD profiles for fresh Mn/NAC, Fe/NAC, MnFe/AC and MnFe/NAC.

Table 3
XPS relative intensity of Mn/NAC, Fe/NAC, MnFe/AC and MnFe/NAC.

Relative intensity (%)		Mn/NAC	Fe/NAC	MnFe/AC	MnFe/NAC	Used MnFe/NAC	
						Hg^0	Hg^0+SO_2
O 1 s	O_L	51.23	59.89	49.01	37.63	57.92	-
	C=O	24.29	16.10	19.01	26.50	14.92	-
	C-O	9.98	11.39	18.38	18.07	17.21	-
	COO-	9.72	8.42	8.73	12.00	5.31	-
	O_{ads}	4.78	4.20	4.87	5.80	4.64	-
[c] Mn 2p	Mn^{2+}	24.35	-	29.97	23.00	24.87	37.53
	Mn^{3+}	47.17	-	45.41	43.02	54.40	45.46
	Mn^{4+}	28.48	-	24.62	33.98	20.73	17.01
	Mn^{4+}/Mn^{2+}+Mn^{3+}	0.40	-	0.33	0.52	0.26	0.21
[d] Fe 2p	Fe^{2+}	-	15.66	14.56	13.78	14.02	13.96
	Fe^{3+}	-	84.34	85.44	86.22	85.98	86.05
	Fe^{3+}/Fe^{2+}	-	5.39	5.87	6.26	6.13	6.16
S 2p	S^{2-}	-	-	-	12.68	-	9.89
	S_2^{2-}	-	-	-	31.64	-	17.45
	S^{6+}	-	-	-	55.68	-	72.66
Hg 4 f	Hg $4f_{5/2}$	-	-	-	-	21.08	18.86
	Si 2p	-	-	-	-	45.12	53.73
	Hg $4f_{7/2}$	-	-	-	-	33.80	27.41
[e] Mn/Fe		-	-	-	-	2.44	1.88

[c]: the percent of different valence of Mn in Mn $2p_{3/2}$.
[d]: the percent of different valence of Fe in Fe 2p3/2.
[e]: the molar ratio of Mn/Fe calculated by XPS.

samples, and thus the relevant active oxygen species were more easily initiated and promoted the reaction (Zhao et al., 2020; Harada et al., 2015). As depicted in Fig. 5(d), the oxygen desorbed at the temperature lower than 300 °C was assigned to the weakly adsorbed oxygen (O_I), and the peak at 300-500 °C could be associated with the release of chemisorbed active oxygen species (O_{II}), such as O_2^- and O^- (Zheng et al.,

2016). The oxygen species desorbed at above 500℃ were not taken into consideration due to their high desorption energy. Notably, although with a higher desorption temperature, the greater peak intensity of O_I on MnFe/NAC indicated there existed more adsorbed O_2, which was consistent with its largest O_{ads} detected by XPS. Besides, the cooperative effect of MnO_x-FeO_x contributed to the lowest desorption temperature of O_{II}, which depended on the content of the oxygen-containing functional groups and oxygen vacancies on MnFe/NAC (Castaño et al., 2015). And higher accessible surface area was also beneficial to the generation of chemisorbed oxygen (Kang et al., 2018). Moreover, according to H_2-TPR, the reduction peaks of both chemisorbed oxygen and metal oxides shifted to a lower temperature over MnFe/NAC, indicating the higher activity of chemisorbed oxygen and higher mobility of lattice oxygen on account of the synergy of MnO_x-FeO_x and strong interaction between metal oxides and support (Fig. S2) (Du et al., 2021). Above all, with an excellent oxygen desorption ability and strong reducibility, MnFe/NAC possessed higher oxygen mobility and abundant unstable oxygen species (Zhang et al., 2018).

3.3. Role of $(NH_4)_2S_2O_8$ modification

The Hg^0 breakthrough curves of AC and NAC were showed in Fig. 6 (a). It could be clearly found that the breakthrough rate of AC quickly reached 90% when adsorption proceeded 455 min, and the adsorption capacity was 43.41 μg/g. After $(NH_4)_2S_2O_8$ modification, the adsorption capacity was enhanced up to 120.94 μg/g. With reaction time increased, the adsorption rate of Hg^0 on both AC and NAC decreased sharply and then a gentle increase of breakthrough rate was observed, except for a sudden deactivation at 335 min over AC and at 415 min over NAC, respectively. As temperature rose, the Hg^0 removal efficiency of both AC and NAC were firstly enhanced and then weakened, which reached the maximum of 26.15% and 31.29% at 90 ℃, respectively (Fig. 6(b)). In particular, the promotion effect of $(NH_4)_2S_2O_8$ modification became more obvious at higher temperature. Based on relevant characterization results, $(NH_4)_2S_2O_8$ modification contributed to a larger surface area, developed microporous structure and abundant oxygen-containing functional groups, which accelerated the Hg^0 removal. Nevertheless, how physico-chemical properties promoted Hg^0 capture on NAC when reacted at diverse temperature need to be explored.

Generally speaking, the adsorption of mercury over carbon-based sorbents involves three steps defined as external mass transfer, surface adsorption and intraparticle diffusion. As shown in Table S2 and Fig. S3, the pseudo-first-order, pseudo-second-order, intraparticle diffusion, and Elovich kinetic models were used to fit the dynamic adsorption process of Hg^0. The correlation coefficients (R^2) depicted in Table S2 were close to 0.99, that is, four adsorption kinetic models were applicable to Hg^0

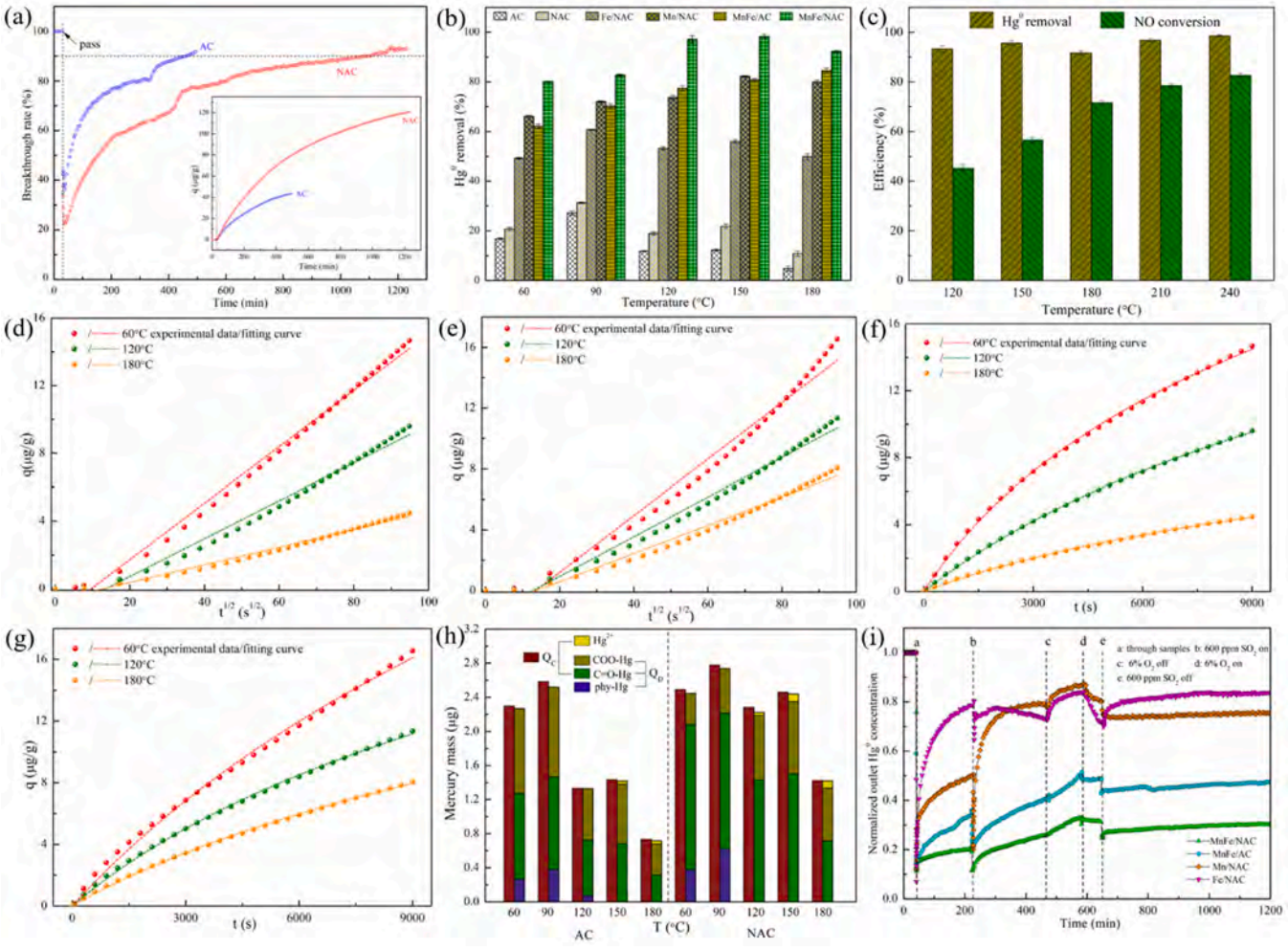

Fig. 6. (a) Hg^0 breakthrough curves and adsorption curves (the insert) of AC and NAC at 35 ℃, (b) Hg^0 removal efficiency over prepared samples at 60-180 ℃, (c) simultaneous removal of Hg^0 and NO from 120 μg/m^3 Hg^0 + 400 ppm NO + 400 ppm NH_3 + 6% O_2/N_2 using MnFe/NAC at 120-240 ℃, (d, e) the fitting curves of intraparticle diffusion model for Hg^0 removal on AC and NAC, (f, g) the fitting curves of Elovich model for Hg^0 removal on AC and NAC, (h) constitution of mercury species of AC and NAC after treated at 60-180 ℃, (i) Hg^0 removal performance at 120 ℃ of samples under different atmospheres (Reaction condition: 0.10-0.15 g sample, 120 μg/m^3 Hg^0 + 0-600 ppm SO_2 + 0-400 ppm NO +0-400 ppm NH_3 + 0-6% O_2/N_2, total flow rate 500 mL/min, reaction time 120 min).

adsorption on AC and NAC at the temperature window. Instead of monolayer adsorption, the adsorption of Hg^0 over samples was proceeded as the combination of physisorption and chemisorption (Cuesta et al. 2012). For Hg^0 removal at 35 ℃, equal R^2 values were calculated for the pseudo-first-order model and pseudo-second-order model. And with reaction temperature rose, a better correlation was observed for the pseudo-second-order model. It demonstrated that external mass transfer and surface adsorption played an equivalent effect on Hg^0 removal at 35 ℃, and chemisorption, as the rate-controlling step, was gradually strengthened with increasing temperature.

As depicted in Fig. 6(d, e), the intraparticle diffusion rate increased with adsorption progressed, while the actual rate showed a decreased tendency, indicating the surface adsorption occurred during Hg^0 capture. Therefore, the initial reaction rate was depended on the surface adsorption rate and intraparticle diffusion rate. At the initial adsorption stage, the existence of plentiful active sites available for Hg^0 adsorption led to the surface adsorption rate being higher than the intraparticle diffusion rate. With the occupancy of limited active sites by mercury, the surface adsorption was limited as revealed by the decreased slope of curves in Fig. S3(a)-(d), and the intraparticle diffusion became operative. After Hg^0 diffused to the sample surface, micropores act as Hg^0 adsorption sites, and mesopores are mainly used as diffusion channels (Hu et al., 2003). And the trend of breakthrough curves at 35 ℃ could be explained. Moreover, NAC possessed a larger k_{id} than AC irrespective of temperature, and it might be resulted from the larger specific surface area and pore volume of NAC, indicating developed porous structure facilitated Hg^0 diffusing in the pores. As a result, NAC possessed a lower breakthrough rate than AC. Notably, with the worst R^2 values, intraparticle diffusion was not the only rate-controlling step for Hg^0 removal.

Notably, Elovich model possessed the best agreement with the experiment data of Hg^0 adsorption, which further verified the predominance of chemisorption on active sites during Hg^0 removal (Fig. 6(f, g)). Meanwhile, the initial mercury adsorption rate, α, was positively correlated with the concentration of oxygen-containing functional groups in the samples. Thus, the promotional effect of $(NH_4)_2S_2O_8$ was contributed to the developed porous structure and abundant oxygen-containing groups, which facilitated the physisorption and chemisorption of Hg^0, respectively. Thereinto, the promotional effect was stronger on the latter than that on the former due to the leading role of chemisorption, and thus resulted in the strengthened facilitation of $(NH_4)_2S_2O_8$ on Hg^0 removal at higher temperature.

To investigate the Hg^0 removal mechanism and distinguish the specific role of active oxygen species during reaction, Hg-TPD was conducted for samples treated with different conditions, which could identify the specific mercury species adsorbed on samples by the desorption temperature. As demonstrated in Fig. S4 and Fig. S5, three

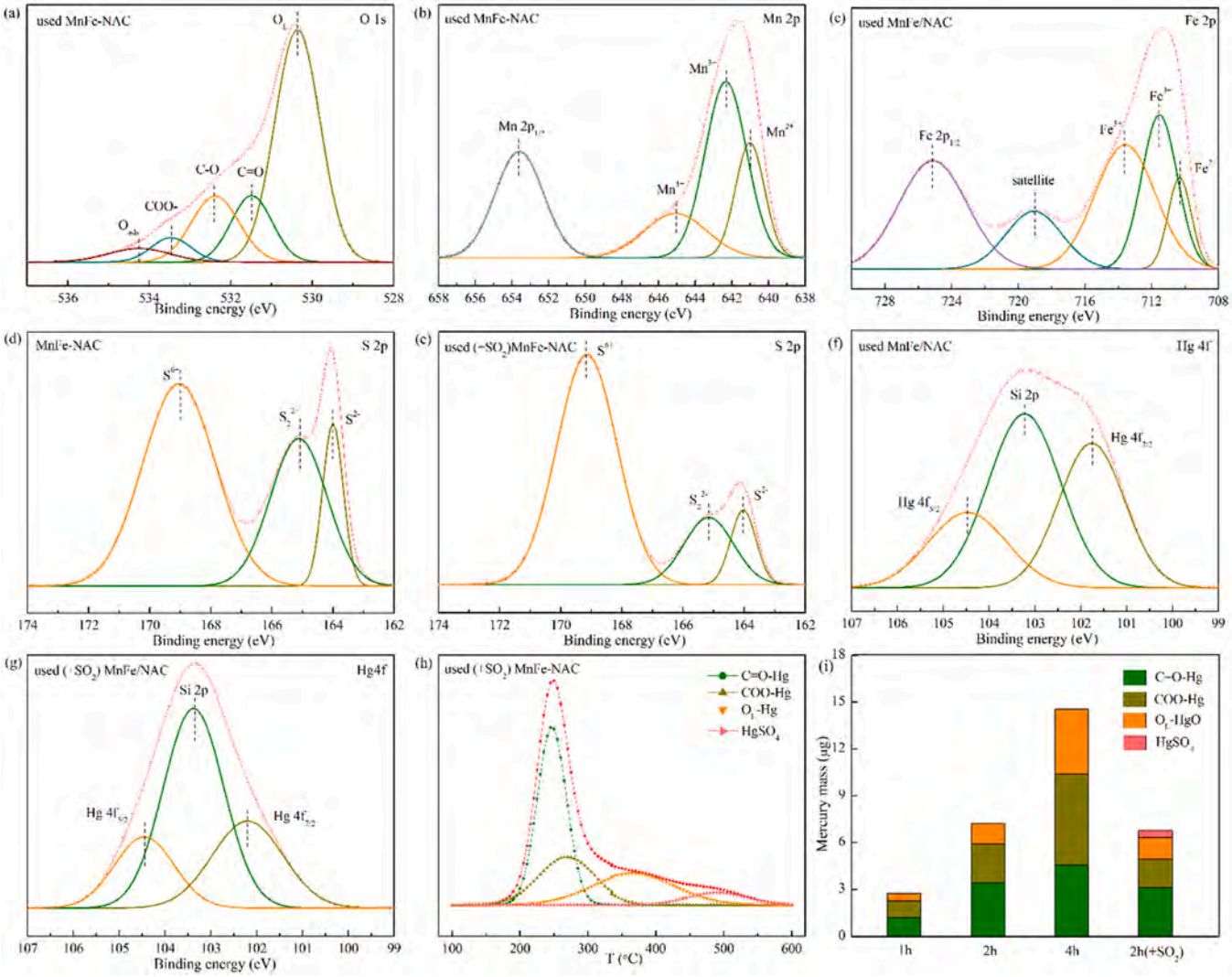

Fig. 7. (a-c) XPS spectra of O 1 s, Mn 2p and Fe 2p on used MnFe/NAC; (d, e) S 2p on fresh and used (+SO_2) MnFe/NAC, (f, g) Hg 4 f on used MnFe/NAC and used (+SO_2) MnFe/NAC, (h) Hg-TPD profile of used (+SO_2) MnFe/NAC and (i) mercury constitution on MnFe/NAC treated for different times.

peaks centered at 170, 245 and 290 ℃ were resolved for both AC and NAC treated at 60 ℃. With temperature elevated, peak I at 170 ℃ disappeared, while peak II and peak III possessed an increased contribution for Hg^0 removal. In combination with kinetic analysis, peak I should be corresponded to the desorption of physical adsorbed mercury, and peak II and peak III should have correlation with chemical adsorbed mercury. Besides, XPS characterization demonstrated that $(NH_4)_2S_2O_8$ modification facilitated the generation of C=O and COO-, and Hg^0 removal efficiency of samples was positively correlated with the amount of C=O and COO-. Moreover, the consumption of C=O and COO- was detected during Hg^0 removal, indicating their participation in Hg^0 removal (Fig. 7 and Table 3). Therefore, peak II and peak III might be ascribed to the desorption of mercury species bonded with ester groups and carbonyl groups. Liu et al. reported that lactone, carbonyl and semiquinone favored the chemisorption of Hg^0, and the adsorption energy of Hg^0 on carbonyl and ester groups was calculated as -137.6 kJ and -164.3 kJ, respectively (Liu et al., 2011). In general, a higher adsorption energy means a higher desorption temperature. Therefore, peak II and peak III were corresponded to the desorption of C=O-Hg and COO-Hg, respectively. In terms of AC, the carbonyl groups predominated in Hg^0 removal at lower temperature and were gradually replaced by ester groups with elevated temperature, while over half of the mercury species was bonded with carbonyl groups over NAC (Fig. 6(h)). Besides, a spot of Hg^{2+} was detected in outlet gas for AC when reacted at 150 and 180 ℃, proving the existence of oxidation during Hg^0 removal. In comparison, NAC possessed a higher oxidation activity for Hg^0 at lower temperature on account of its abundant oxygen functional groups.

Above all, $(NH_4)_2S_2O_8$ modification enhanced Hg^0 removal on AC, and the facilitation was more obvious at higher temperature. Based on characterizations, $(NH_4)_2S_2O_8$ modification endowed NAC with higher surface area, larger pore volume and more active oxygen species, which facilitated the physisorption and chemisorption, respectively. Besides, according to Hg-TPD, Hg^0 removal on both AC and NAC proceeded as the combination of chemisorption, as the predominant role, and physisorption, and strengthened chemisorption and weakened physisorption was observed with temperature elevated. Moreover, the best agreement with Elovich model further confirmed the predominant role of chemisorption during Hg^0 removal. Therefore, $(NH_4)_2S_2O_8$ doping accelerated Hg^0 removal via the optimization on porous structure and oxygen functional groups, and a stronger promotional effect of $(NH_4)_2S_2O_8$ modification was detected for chemisorption of Hg^0.

3.4. Activity of MnO_x-FeO_x impregnated samples

3.4.1. Hg^0 removal performance

The activity of modified activated coke for Hg^0 removal was investigated at 60-180 ℃. As demonstrated in Fig. 6(b), the impregnation of FeO_x or MnO_x improved the activity of NAC to a large extent, as identified by a sharp increase of Hg^0 removal efficiency higher than 30% and 40%, respectively. It should be noticed that different from Fe/NAC possessing similar tendency with AC and NAC, Mn/NAC exhibited superior Hg^0 removal performance at higher temperature. The difference was plausibly owing to the higher S_{BET} and V_p of Fe/NAC and abundant oxygen species of Mn/NAC, which benefited for the physisorption and chemisorption of Hg^0, respectively. Therefore, the cooperation of MnO_x-FeO_x on NAC support contributed to excellent Hg^0 removal efficiency higher than 80% at the whole temperature, which even exceeded 90% when the temperature elevated above 120 ℃. Besides, the highest R^2 (>0.999) of Elovich model indicated chemisorption predominated in Hg^0 removal over MnFe/NAC (Fig. S3(f)). Increasing temperature could boost the diffusion of gas reactants, and lead to a lower activation energy barrier for Hg^0 adsorption, hence enhancing the Hg^0 removal performance (Liu et al., 2020a). With the same content of MnO_x-FeO_x, the sample with AC support exhibited lower activity than MnFe/NAC irrespective of reaction temperature. On one hand, the formation of more micropores owing to $(NH_4)_2S_2O_8$ modification provided more active sites for Hg^0 and O_2 adsorption, as well as the dispersion of active components. And more mesopores was in favor for Hg^0 diffusion. On the other hand, higher oxygen mobility and abundant unstable oxygen species contributed to the chemisorption of Hg^0 over MnFe/NAC. Above all, the optimal working temperature for MnFe/NAC was 120-180 ℃, which matched well with the temperature of flue gas between the air preheater and the electrostatic precipitator (Liu et al., 2020a).

3.4.2. Simultaneous removal of Hg^0 and NO

Furthermore, the activity of MnFe/NAC for simultaneous removal of Hg^0 and NO was also tested. MnFe/NAC exhibited superior Hg^0 removal efficiency above 90% at 120~240 ℃, and only a slight decrease was detected after injecting 400 ppm NO and 400 ppm NH_3. Thereinto, the lowest activity was observed when reacted at 180 ℃, which might be due to the weakened adsorption and enhanced oxidation with increased temperature. However, NO conversion was more sensitive to the varied temperature. As temperature increased, the NO conversion efficiency enhanced from 45.25% to 82.65%. Notably, an enhancement of 16.37% was detected when temperature elevated from 120 ℃ to 180 ℃. A higher temperature could not only provide more kinetic energy for reaction, but also benefit for the activation of oxygen and thus generated more active oxygen species for SCR reaction (Zhu et al., 2019). Therefore, MnFe/NAC exhibited the best activity at 240 ℃, which possessed 98.54% Hg^0 removal efficiency and 82.65% NO conversion efficiency comparable to some SCR catalysts.

3.5. Effect of gas components

3.5.1. Effect of SO_2

As a curial factor to appraise the potential of absorbents in practical application, the SO_2-resistance of samples for Hg^0 removal was studied. As shown in Fig. 6(i), with the addition of 600 ppm SO_2, the activity of Mn/NAC, MnFe/AC and MnFe/NAC for Hg^0 removal were weakened to some extent. Especially, the Hg^0 removal efficiency on Mn/NAC decreased from 49.36% to 19.89% after injecting SO_2. It's worth noting that an enhancement, rather than inhibition, was observed for Hg^0 removal on Fe/NAC with SO_2 addition, in which the adsorbed SO_2 could effectively act as capture site for Hg^0. Besides, the incorporation of FeO_x on Mn/NAC improved the SO_2-resistance significantly, and only a slight decrease of 10% on Hg^0 removal efficiency was observed for MnFe/NAC after long-term SO_2-resistance test. Besides, when cutting off O_2, a decreased tendency of Hg^0 removal efficiency was observed for all samples. After adding O_2 again, the Hg^0 removal efficiency was recovered to some extent, since some consumed active oxygen species could be regenerated with the aid of gaseous oxygen. However, for Mn/NAC, MnFe/AC and MnFe/NAC, the cut-off of SO_2 brought about a slight enhancement of Hg^0 removal efficiency, demonstrating the irreversible poisoning effect on sample caused by SO_2. On the contrary, the absence of SO_2 led to the worse performance for Hg^0 removal on Fe/NAC.

According to previous researches, three aspects should be responsible for the suppression of SO_2 on Hg^0 removal: (1) the competitive adsorption occurred between SO_2 and Hg^0 on active site (Li et al., 2019; Yang et al., 2018); (2) the poisoning of metal oxides via the formation of sulphate or sulphite (He et al., 2016; Xu et al., 2016); (3) the consumption of oxygen functional groups by SO_2 (Zhang et al., 2020). In our work, the irreversible decline of Hg^0 removal efficiency after cutting off SO_2 implied the occurrence of some changes in the surface chemistry characteristics of samples, such as the sulfation of metal oxides, and the competitive adsorption was not the determining role in the weakened Hg^0 removal with additive SO_2 (Wang et al., 2020b). Meanwhile, based on the O_2-transient response test with the presence of SO_2, it could be deduced the occupancy of oxygen-containing functional groups by SO_2 resulted in the deactivation of samples. As reported by Fang and Li, C=O, COOH and C-O could act as the active center for SO_2 oxidation and promote the removal of SO_2 (Fang et al., 2017; Li et al., 2017). With higher concentration and stronger affinity to AC surface, SO_2 was

preferential to combined with the oxygen-containing functional groups, while the occupied active oxygen species were not available for Hg^0 adsorption and oxidation. More in-depth discussion would be conducted in the following part.

3.5.2. Effect of H_2O and HCl

As depicted in Fig. S6, how H_2O and HCl affected on Hg^0 removal was also explored. 8 vol% H_2O addition only led to a slight decrease of 2.20%, and the inherent hydrophobicity of activated coke endowed MnFe/NAC with a superior H_2O-resistance. Besides, the coexistence of 600 ppm SO_2 and 8 vol% H_2O further strengthened the inhibition, as demonstrated by Hg^0 removal efficiency declined by 6.85%. The boosting competitive adsorption of SO_2/H_2O with Hg^0 on active sites should responsible for it. Moreover, when adding 10 ppm HCl into SFG (120 μg/m^3 Hg^0 + 600 ppm SO_2 + 6% O_2 + 8 vol.% H_2O/N_2), ~100% Hg^0 removal efficiency was reached beyond all doubt. On one hand, HCl could reacted with the HgO adsorbed on sample directly and formed $HgCl_2$. On the other hand, after adsorbed on samples, HCl_{ads} could be activated by active oxygen species, the generated active chlorine species (Cl*) would oxidized Hg^0_{ads} into HgCl and $HgCl_2$ (Wang et al., 2021). Above all, MnFe/NAC possessed a superior resistance to SO_2 and H_2O, which was of great significance in practical application.

3.6. Mechanism discussion

On the basis of XPS, FTIR and Hg-TPD, the mechanism concerning Hg^0 removal on MnFe/NAC at different atmospheres was discussed. As summarized in Fig. 7 and Table 3, the consumption of C=O, COO- and O_{ads} were observed for MnFe/NAC after exposure to Hg^0+O_2/N_2, while O_L was endowed with an increased ratio. Similar results was also found for FTIR spectra, in which the peaks relevant to C=O (1735 cm^{-1}, 1558 cm^{-1}, 1468 cm^{-1}) and COO- (1080 cm^{-1}) on used MnFe/NAC weakened significantly when comparing with fresh MnFe/NAC (Fig. S7) (Zhang et al., 2015; Terzyk, 2001). In particular, the decline of 11.58% and 6.69% for C=O and COO- further proved the assumption that mercury species existed in the form of C=O-Hg and COO-Hg over samples. Besides, the Hg^0 removal led to the reduction of metal atoms with high valence, indicating their participation in Hg^0 removal. However, the decreased Mn^{4+}, Mn^{3+} and Fe^{3+} seemed to be in contradiction with the increased O_L. The formation of Hg^{2+} over used MnFe/NAC might account for the increased lattice oxygen, as demonstrated by the appearance of two new peaks at 101.80 and 104.38 eV for Hg 4 f spectra. Furthermore, Hg-TPD was conducted to explore whether O_L involved in Hg^0 removal. As depicted in Fig. S8, an additional peak at around 380 ℃ was observed on used MnFe/NAC, which was considered as the desorption of mercury species bonded with O_L (Du et al., 2021). Accordingly, both oxygen-containing functional groups and lattice oxygen participated in Hg^0 removal on MnFe/NAC. Meanwhile, with the reaction time prolonged, three mercury species adsorbed on sample were gradually accumulated with diverse tendencies (Fig. 7(i) and Fig. S8). The content of COO-Hg and O_L-HgO exhibited an increased slop versus reaction time, and an increase of 3.31 μg and 2.87 μg was observed when the response time was extended from 2 h to 4 h, respectively. Differently, as the main active site for mercury over MnFe/NAC at the initial stage of reaction, there was a slight growth of C=O-Hg for the further reaction. Therefore, it could be deduced that the priority of active oxygen species for Hg^0 removal on MnFe/NAC at 120 ℃ was as follows: carbonyl group > ester group > lattice oxygen.

When adding 600 ppm SO_2 in simulated flue gas, 72.66% of sulfur elements existed in the form of S^{6+}, which was higher than that in fresh MnFe/NAC. Two reaction pathways might contribute to the formation of SO_4^{2-}. On one hand, the sharp decrease of Mn/Fe molar ratio and more Mn^{2+} on the surface of used (+SO_2) MnFe/NAC calculated by XPS indicated the formation of $MnSO_4$, which was easier to be agglomerated on the surface and pores of MnFe/NAC (Table 3) (Hamzehlouyan et al., 2016). Besides, the slight increase of Fe^{3+}/Fe^{2+} manifested the absence of sulfation of FeO_x with SO_2 addition. On the other hand, the desorption peak at around 490 ℃ for used (+SO_2) MnFe/NAC was relevant to the formation of $HgSO_4$ via Hg^0_{ads}+ 2 O* + SO_2 → $HgSO_4$ (Li et al., 2017; Wu et al., 2019) (Fig. 7(h)). As shown in Fig. S9, SO_2 addition accelerated the Hg^0 adsorption on active oxygen species of Fe/NAC, especially for C=O-Hg, while the decreased C=O-Hg and COO-Hg, as well as a slight weakened O_L-HgO, were observed for used (+SO_2) Mn/NAC. In general, C=O, with Brønsted basic properties, possessed a higher affinity for SO_2 than Hg^0, and thus preferentially acted as active sites for SO_2. With the top priority for Hg^0 removal, the occupancy of C=O by SO_2 resulted in the inferior activity of Mn/NAC. In terms of MnFe/NAC, the suppression of SO_2 on C=O-Hg and COO-Hg was weakened to a large extent with the incorporation of FeO_x. Above all, the promotional Hg^0 removal on Fe/NAC with the aid of SO_2 was ascribed to the stimulative Hg^0 adsorption on active oxygen species and the formation of SO_4^{2-}, which acted as new active sites for Hg^0 removal, rather than brought about the sulfation of FeO_x. On the contrary, the poisoning effect of SO_2 on Hg^0 capture over MnFe/NAC was mainly proceeded as the combination of sulfation of MnO_x and occupancy of C=O and COO- by SO_2, which became deactivated for Hg^0 removal, and the cooperation of FeO_x improved the SO_2-resistance of sample through weakening the adsorption of SO_2 on samples via oxygen functional groups.

On the basis of above experiment and characterization results, the mechanism relevant to Hg^0 removal on MnFe/NAC was proposed in Fig. 8. The Hg^0 in flue gas was firstly adsorbed on surface of sample via two methods: physisorption and chemisorption. Physisorption usually occurred at lower temperature (such as ≤ 90 ℃) via van der Waals forces, in which the well-developed microporous structure and larger fractal dimension worked. On the other hand, the oxidation of $(NH_4)_2S_2O_8$ and further impregnation of MnO_x-FeO_x endowed MnFe/NAC with more active oxygen species for chemisorption of Hg^0 on sample. Thereinto, the priority of active oxygen species for Hg^0 chemisorption was as follows: C=O > COO- > O_L. Meanwhile, part of Hg^0 would be oxidized into Hg^{2+} and desorbed from sample, as identified by the Hg^{2+} detected from outlet flue gas. During the process, the active oxygen species consumed could be replenished by gaseous continuously. The SO_2 addition exhibited a slight inhibition on Hg^0 removal through the deactivation of MnO_x and the occupation of C=O and COO-, and the FeO_x addition could weakened the adsorption of SO_2 on samples via oxygen functional groups.

4. Regeneration performance

As one of curial factor in practical application, regeneration performance of MnFe/NAC was evaluated. As depicted in Fig. 9(a), no obvious deactivation was observed after five recycle, and the sample exhibited the highest removal efficiency of 97.92% in 3th recycle. It elucidated that the thermal treatment could efficiently recover the active sites occupied by mercury. Besides, the development of pore structure and the intrinsic chain scission of macromolecules during thermal regeneration were in favor of the adsorption and oxidation of Hg^0. Moreover, irrespectively of SO_2 addition, MnFe/NAC exhibited an excellent stability, which further testified the great potential in practical application (Fig. S12). When in the absence of O_2, the activity of MnFe/NAC deteriorated sharply, with the decrease higher than 10%, after regeneration except for the fourth run. The replenishment of active oxygen species by gaseous oxygen was the principal factor for superior activity of MnFe/NAC. As depicted in the transient response test to oxygen (Fig. 9(c)), it could be clearly found that after the treatment in Fig. 9(b), the addition of oxygen still could enhance the Hg^0 removal efficiency from 40.28% to 76.43%, and no obvious impairment was detected when decreasing the oxygen concentration from 6% to 3%. Once cutting off O_2, the Hg^0 removal efficiency of MnFe/NAC decreased to 47.25%, further illustrating the motivation of oxygen during Hg^0 capture. The compositions of mercury species on MnFe/NAC during each regeneration were compared in Fig. 9(d) and Fig. S10-S11. With the participation of O_2

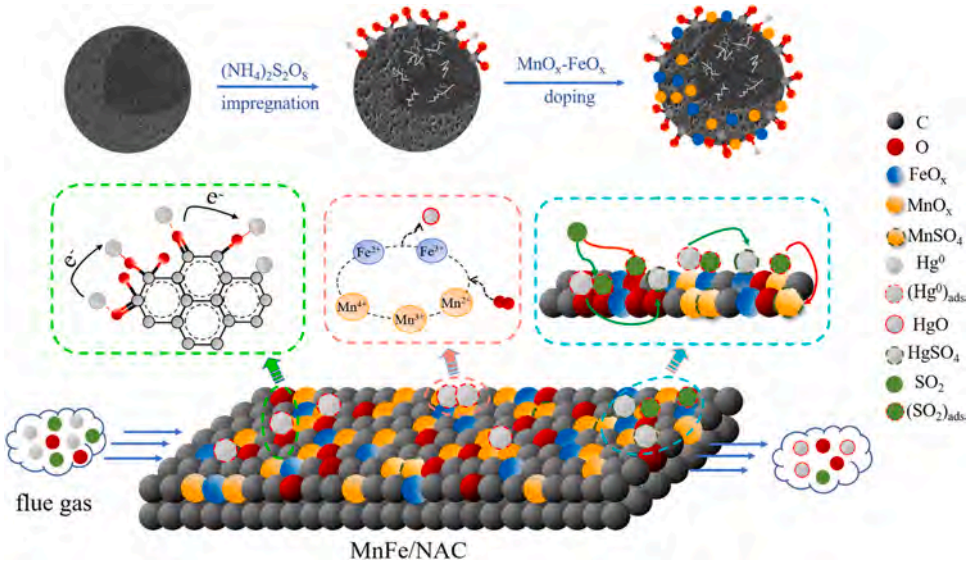

Fig. 8. The proposed mechanism of Hg^0 removal over MnFe/NAC.

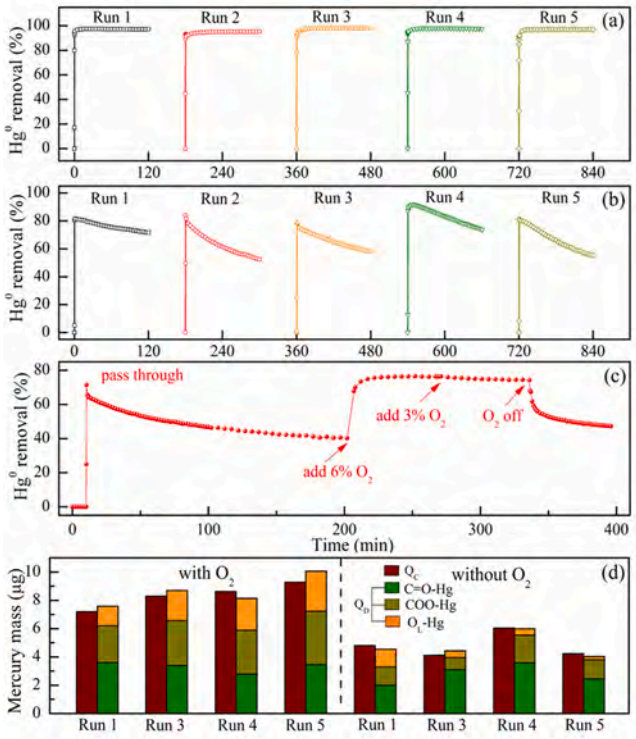

Fig. 9. The regeneration performance of MnFe/NAC with exposure to (a) 120 μg/m^3 Hg^0 + 6% O_2/N_2, (b) 120 μg/m^3 Hg^0/N_2, (c) transient response test to oxygen and (d) the constitution of mercury species on regenerated MnFe/NAC according to Hg-TPD.

during Hg^0 removal, a decreased ratio of C=O-Hg and an increased ratio of COO-Hg and O_L-Hg were detected as regeneration frequency increased. When cut off O_2, all mercury species were observed with a lower mass. Besides, the proportion of mercury bonded with COO- and O_L was weakened, and, especially, the formation of O_L-HgO was weakened significantly. However, C=O-Hg formed on MnFe/NAC possessed a higher proportion. Once the mercury species bonded with lattice oxygen were released, the lattice oxygen could not be recovered, and the gaseous oxygen could effectively restore the consumed lattice oxygen to some extent (Xu et al., 2021). Differently, some oxygen functional groups could be regenerated during thermal treatment and acted as capture sites for the following Hg^0 removal. Besides, the decomposition of macromolecules when heating also contributed to the generation of oxygen containing functional groups. Therefore, the motivation of O_2 was in favor of the adsorption of Hg^0 on active oxygen species, especially for the regeneration of the regeneration of lattice oxygen species via the reoxidation of metal ions.

5. Conclusion

In this study, $(NH_4)_2S_2O_8$ impregnation and the subsequent loading of MnO_x-FeO_x were performed for the optimization of activated coke used in Hg^0 removal from simulated flue gas. The obtained MnFe/NAC exhibited excellent activity as revealed by the Hg^0 removal efficiency higher than 90% at a broad temperature window of 120~180 ℃, as well as superior performance for simultaneous removal of Hg^0 and NO, and outstanding resistance to SO_2 and H_2O. According to characterizations, $(NH_4)_2S_2O_8$ modification led to well-developed microporous structures and abundant oxygen-containing functional groups, and thus provided more active sites for metal oxides doping and gaseous reactants adsorption. With strong synergy of MnO_x-FeO_x and interaction between metal oxides and support, MnFe/NAC possessed stronger reducibility, plentiful active oxygen species with higher mobility and metal ions with higher valence, and thus contributed to its superior activity. Hg-TPD revealed that the mercury species adsorbed on MnFe/NAC mainly existed as phy-Hg, C=O-Hg, COO-Hg and O_L-HgO, and a small quantity of Hg^{2+} were also detected in outlet flue gas. Meanwhile, as the dominant role in Hg^0 removal, chemisorption of Hg^0 on active oxygen species followed the order of precedence: C=O> COO->O_L. Besides, SO_2-poisioning effect mainly occurred as the deactivation of MnO_x and occupancy of oxygen functional groups, while the FeO_x cooperation weakened the SO_2 adsorption on oxygen functional groups effectively. And O_2 motivated the Hg^0 removal mainly through Hg^0 adsorption on active oxygen species, especially on O_L. Furthermore, the superior regeneration performance, excellent stability of MnFe/NAC indicated its potential in industrial application.

Environmental implication

With high toxicity, long-distance migration and bioaccumulation, Hg^0 is harmful to human health and environment. Based on the existing desulfurization devices using activated coke (AC), MnO_x-FeO_x/$(NH_4)_2S_2O_8$-AC was prepared for boosting Hg^0 removal and SO_2-

resistance via tunning active oxygen species innovatively. How $(NH_4)_2S_2O_8$ impregnation and MnO_x-FeO_x doping affected the physicochemical properties, activity and SO_2-resistance was illuminated. Besides, the specific role of diverse active oxygen species during Hg^0 removal was also distinguished. The work provided the theoretical foundation for the targeted adjustment of physicochemical properties of AC for efficient control of Hg^0 emission in industrial application.

CRediT authorship contribution statement

Xueyu Du: Conceptualization, Methodology, Investigation, Writing - original draft, Data curation, Validation. **Caiting Li:** Conceptualization, Supervision, Writing - review & editing, Funding acquisition. **Jie Zhang:** Methodology, Investigation, Writing - review & editing. **Youcai Zhu:** Methodology. **Caixia Liang:** Writing - review & editing. **Le Huang:** Writing - review & editing. **Kuang Yang:** Writing - review & editing. **Chaoliang Yao:** Methodology. **Ying Ma:** Methodology.

Declaration of Competing Interest

The authors declare that they have no known competing financial interests or personal relationships that could have appeared to influence the work reported in this paper.

Data availability

The data that has been used is confidential.

Acknowledgment

This work was financially supported by the National Key Research and Development Program of China (2016YFC0204100) and the Scientific and Technological Major Special Project of Changsha City in China (KQ1201011).

Appendix A. Supporting information

Supplementary data associated with this article can be found in the online version at doi:10.1016/j.jhazmat.2022.129882.

References

Avnir, D., Farin, D., Pfeifer, P., 1983. Chemistry in noninteger dimensions between two and three. II. Fractal surfaces of adsorbents. J. Chem. Phys 79, 3566–3571.

Castaño, M.H., Molina, R., Moreno, S., 2015. Cooperative effect of the Co–Mn mixed oxides for the catalytic oxidation of VOCs: influence of the synthesis method. Appl. Catal. A: Gene. 492, 48–59. https://doi.org/10.1016/j.apcata.2014.12.009.

Chen, J.Q., Li, C.T., Li, S.H., Lu, P., Gao, L., Du, X.Y., Yi, Y.Y., 2018. Simultaneous removal of HCHO and elemental mercury from flue gas over Co-Ce oxides supported on activated coke impregnated by sulfuric acid. Chem. Eng. J. 338, 358–368. https://doi.org/10.1016/j.cej.2018.01.043.

Chen, W.M., Pei, Y., Huang, W.J., Qu, Z., Hu, X.F., Yan, N.Q., 2016. Novel effective catalyst for elemental mercury removal from coal-fired flue gas and the mechanism investigation. Environ. Sci. Technol. 50, 2564–2572. https://doi.org/10.1021/acs.est.5b05564.

Cuesta, A.F., Somoano, M.D., Anton, M.A.L., Cieplik, M., Fierro, J.L., Tarazona, M.R.M., 2012. Biomass gasification chars for mercury capture from a simulated flue gas of coal combustion. J. Environ. Manage. 98, 23–28. https://doi.org/10.1016/j.jenvman.2011.12.013.

Diagboya, P.N., Olu-Owolabi, B.I., Adebowale, K.O., 2015. Synthesis of covalently bonded graphene oxide–iron magnetic nanoparticles and the kinetics of mercury removal. RSC Adv 5, 2536–2542. https://doi.org/10.1039/c4ra13126f.

Dong, L., Huang, Y.J., Liu, L.Q., Liu, C.Q., Xu, L.G., Zha, J.R., Chen, H., Liu, H., 2019. Investigation of elemental mercury removal from coal-fired boiler flue gas over MIL101-Cr. Energy Fuels 33, 8864–8875. https://doi.org/10.1021/acs.energyfuels.9b01355.

Du, X.Y., Li, C.T., Zhao, L.K., Zhang, J., Gao, L., Sheng, J.J., Yi, Y.Y., Chen, J.Q., Zeng, G.M., 2018. Promotional removal of HCHO from simulated flue gas over Mn-Fe oxides modified activated coke. Appl. Catal. B: Environ. 232, 37–48. https://doi.org/10.1016/j.apcatb.2018.03.034.

Du, X.Y., Li, C.T., Zhang, J., Zhao, L.K., Li, S.H., Lyu, Y., Zhang, Y.D., Zhu, Y.C., Huang, L., 2021. Highly efficient simultaneous removal of HCHO and elemental mercury over Mn-Co oxides promoted Zr-AC samples. J. Hazard. Mater. 408, 124830 https://doi.org/10.1016/j.jhazmat.2020.124830.

Emission Standard of Air Pollutants for Thermal Power Plants, GB13223-2011, MEP of China: Beijing, China, (2011).

Fan, X.P., Li, C.T., Zeng, G.M., Gao, Z., Chen, L., Zhang, W., Gao, H.L., 2010. Removal of gas-phase element mercury by activated carbon fiber impregnated with CeO_2. Energy Fuels 24, 4250–4254. https://doi.org/10.1021/ef100377f.

Fang, N.J., Guo, J.X., Shu, S., Li, J.J., Chu, Y.H., 2017. Influence of textures, oxygen-containing functional groups and metal species on SO_2 and NO removal over Ce-Mn/NAC. Fuel 202, 328–337. https://doi.org/10.1016/j.fuel.2017.04.035.

Hamzehlouyan, T., Sampara, C.S., Li, J.H., Kumar, A., Epling, W.S., 2016. Kinetic study of adsorption and desorption of SO_2 over γ-Al_2O_3 and Pt/γ-Al_2O_3. Appl. Catal. B: Environ. s 181, 587–598. https://doi.org/10.1016/j.apcatb.2015.08.003.

Harada, K., Oishi, T., Hamamoto, S., Kawasaki, T., Ishihara, T., 2015. Oxygen desorption properties of Pr_6O_{11} doped with Bi and Ce for low temperature particulate matter oxidation. Appl. Cataly. A: Gene. 492, 223–230. https://doi.org/10.1016/j.apcata.2014.12.036.

He, C., Shen, B.X., Li, F.K., 2016. Effects of flue gas components on removal of elemental mercury over Ce-MnO_x/Ti-PILCs. J. Hazard. Mater. 304, 10–17. https://doi.org/10.1016/j.jhazmat.2015.10.044.

Hong, Q.Y., Liao, Y., Xu, H.M., Huang, W.J., Qu, Z., Yan, N.Q., 2020. Stepwise ions incorporation method for continuously activating PbS to recover mercury from Hg^0-rich flue gas. Environ. Sci. Technol 54, 11594–11601. https://doi.org/10.1021/acs.est.0c03335.

Hu, Z.H., Guo, H.M., Srinivasan, M.P., Ni, Y.M., 2003. A simple method for developing mesoporosity in activated carbon. Sep. Purif. Technol. 31, 47–52. https://doi.org/10.1016/S1383-5866(02)00148-X.

Kang, L., Han, L.P., Wang, P.L., Feng, C., Zhang, J.P., Yan, T.T., Deng, J., Shi, L.Y., Zhang, D.S., 2020. SO_2-tolerant NO_x reduction by marvelously suppressing SO_2 adsorption over $Fe_8Ce_{1-\delta}VO_4$ catalysts. Environ. Sci. Technol. 54, 14066–14075. https://doi.org/10.1021/acs.est.0c05038.

Kang, R.N., Wei, X.L., Bin, F., Wang, Z.B., Hao, Q.L., Dou, B.J., 2018. Reaction mechanism and kinetics of CO oxidation over a $CuO/Ce_{0.75}Zr_{0.25}O_{2-\delta}$ catalyst. Appl. Catal. A: Gene. 565, 46–58. https://doi.org/10.1016/j.apcata.2018.07.026.

Kong, L.N., Zou, S.J., Mei, J., Geng, Y., Zhao, H., Yang, S.J., 2018. Outstanding resistance of H_2S-modified Cu/TiO_2 to SO_2 for capturing gaseous Hg^0 from nonferrous metal smelting flue gas: Performance and reaction mechanism. Environ. Sci. Technol. 52, 10003–10010 https://doi.org /10.1021/acs.est.8b03484.

Jampaiah, D., Chalkidis, A., Sabri, Y.M., Mayes, E.L.H., Reddy, B.M., Bhargava, S.K., 2019. Low-temperature elemental mercury removal over TiO_2 nanorods-supported MnO_x-FeO_x-CrO_x. Catalysis Today 324, 174–182. https://doi.org/10.1016/j.cattod.2018.11.049.

Li, G.L., Wang, S.X., Wu, Q.R., Li, J.H., You, X.Q., Shao, S., Liu, K.Y., 2019. Exploration of reaction mechanism between acid gases and elemental mercury on the CeO_2–WO_3/TiO_2 catalyst via in situ DRIFTS. Fuel 239, 162–172. https://doi.org/10.1016/j.fuel.2018.10.142.

Li, J.Y., Wu, Q.R., Wang, Y.Y., Chang, H.Z., Ma, L., 2020. Improvement of NH_3 resistance over CuO/TiO_2 catalysts for elemental mercury oxidation in a wide temperature range. Catalysis Today 376, 276–284. https://doi.org/10.1016/j.cattod.2020.05.029.

Li, Y.N., Duan, Y.F., Wang, H., Zhao, S.L., Chen, M.M., Liu, M., Wei, H.Q., 2017. Effects of acidic gases on mercury adsorption by activated carbon in simulated oxy-fuel combustion flue gas. Energy Fuels 31, 9745–9751. https://doi.org/10.1021/acs.energyfuels.7b01480.

Liu, D.J., Lu, C., Wu, J., 2018. Gaseous mercury capture by copper-activated nanoporous carbon nitride. Energy Fuels 32, 8287–8295. https://doi.org/10.1021/acs.energyfuels.8b01708.

Liu, D.J., Zhang, Z., Wu, J., 2019a. Elemental mercury removal by MnO_2 nanoparticle-decorated carbon nitride nanosheet. Energy Fuels 33, 3089–3097. https://doi.org/10.1021/acs.energyfuels.9b00149.

Liu, D.J., Zhang, Z., Luo, F., Wu, J., 2020a. Elemental mercury capture from simulated flue gas by graphite-phase carbon nitride. Energy Fuels 34, 6851–6861. https://doi.org/10.1021/acs.energyfuels.0c00457.

Liu, J., Cheney, M.A., Wu, F., Li, M., 2011. Effects of chemical functional groups on elemental mercury adsorption on carbonaceous surfaces. J. Hazard. Mater. 186, 108–113. https://doi.org/10.1016/j.jhazmat.2010.10.089.

Liu, L.Z., Sun, J.T., Ding, J.D., Zhang, Y., Sun, T.H., Jia, J.P., 2019b. Highly active $Mn_{3-x}Fe_xO_4$ spinel with defects for toluene mineralization: insights into regulation of the oxygen vacancy and active metals. Inorg. Chem 58, 13241–13249. https://doi.org/10.1021/acs.inorgchem.9b02105.

Liu, M., Li, C.T., Zeng, Q., Du, X.Y., Gao, L., Li, S.H., Zhai, Y.B., 2019c. Study on removal of elemental mercury over MoO_3-CeO_2/cylindrical activated coke in the presence of SO_2 by Hg-temperature-programmed desorption. Chem. Eng. J. 371, 666–678. https://doi.org/10.1016/j.cej.2019.04.088.

Liu, Z., Liu, D.Y., Zhao, B.T., Feng, L., Ni, M.G., Jin, J., 2020b. Mercury removal based on adsorption and oxidation by fly ash: a review. Energy Fuels 34, 11840–11866. https://doi.org/10.1021/acs.energyfuels.0c02209.

Ma, X.Y., Hao, R.L., Wang, Z.Y., Xu, P.Y., Luo, Y.C., Zhao, Y., 2020. Nanoscale $CuFe_2O_4$ monodispersedly anchored on reduced graphene oxide as excellent peroxydisulfate catalyst for removal of gaseous elemental mercury. Chem. Eng. J. 401, 126101 https://doi.org/10.1016/j.cej.2020.126101.

Ma, Y.P., Xu, T.F., Zhang, X.J., Fei, Z.H., Zhang, H.Z., Xu, H.M., Ma, Y.X., 2021. Manganese bridge of mercury and oxygen for elemental mercury capture from industrial flue gas in layered Mn/MCM-22 zeolite. Fuel 283, 118973. https://doi.org/10.1016/j.fuel.2020.118973.

Pirrone, N., Cinnirella, S., Feng, X., Finkelman, R.B., Friedli, H.R., Leaner, J., Mason, R., Mukherjee, A.B., Stracher, G.B., Streets, D.G., Telmer, K., 2010. Global mercury emissions to the atmosphere from anthropogenic and natural sources. Atmos. Chem. Phy. 10, 5951–5964. https://doi.org/10.5194/acp-10-5951-2010.

Shen, B.X., Liu, T., Zhao, N., Yang, X.Y., Deng, L.D., 2010. Iron-doped Mn-Ce/TiO_2 catalyst for low temperature selective catalytic reduction of NO with NH_3. J. Environ. Sci. 22, 1447–1454. https://doi.org/10.1016/S1001-0742(09)60274-6.

Shen, W.Z., Li, Z.J., Liu, Y.H., 2008. Surface chemical functional groups modification of porous carbon. Recent Pat. on Chem. Eng. 1, 27–40. https://doi.org/10.2174/1874478810801010027.

Shen, Y.F., Zhao, P.T., Shao, Q.F., Ma, D.C., Takahashi, F., Yoshikawa, K., 2014. In-situ catalytic conversion of tar using rice husk char-supported nickel-iron catalysts for biomass pyrolysis/gasification. Appl. Catal. B: Environ. 152-153, 140–151. https://doi.org/10.1016/j.apcatb.2014.01.032.

Simonin, J.P., 2016. On the comparison of pseudo-first order and pseudo-second order rate laws in the modeling of adsorption kinetics. Chem. Eng. J. 300, 254–263. https://doi.org/10.1016/j.cej.2016.04.079.

Streets, D.G., Horowitz, H.M., Jacob, D.J., Lu, Z.F., Levin, L., Schure, A.F.H., Sunderland, E.M., 2017. Total mercury released to the environment by human activities. Environ. Sci. Technol. 51, 5969–5977. https://doi.org/10.1021/acs.est.7b00451.

Tan, Z.Q., Su, S., Qiu, J.R., Kong, F.H., Wang, Z.A., Hao, F., Xiang, J., 2012. Preparation and characterization of Fe_2O_3–SiO_2 composite and its effect on elemental mercury removal. Chem. Eng. J. 195-196, 218–225 http:// doi.org/10.1016/j.cej.2012.04.083.

Terzyk, A.P., 2001. The influence of activated carbon surface chemical composition on the adsorption of acetaminophen (paracetamol) in vitro Part II. TG, FTIR, and XPS analysis of carbons and the temperature dependence of adsorption kinetics at the neutral pH. Colloid. Surface. A 177, 23–45.

Wang, C., Hong, Q.Q., Ma, C., Mei, J., Yang, S.J., 2021. Novel promotion of sulfuration for Hg^0 conversion over V_2O_5-MoO_3/TiO_2 with HCl at low temperature: Hg^0 adsorption, Hg^0 oxidation, and Hg^{2+} adsorption. Environ. Sci. Technol. 55, 7072–7081. https://doi.org/10.1021/acs.est.1c00828.

Wang, J., Meng, X., Chen, J., Yu, Y., Miao, J., Yu, W., Xie, Z., 2016. Desulphurization performance and mechanism study by in situ DRIFTS of activated coke modified by oxidization. Ind. Eng. Chem. Res. 55, 3790–3796. https://doi.org/10.1021/acs.iecr.6b00210.

Wang, L.W., Hou, D.Y., Cao, Y.N., Ok, Y.S., Tack, F.M.G., Rinklebe, J., O'Connor, D., 2020a. Remediation of mercury contaminated soil, water, and air: A review of emerging materials and innovative technologies. Environ. Int. 134, 105281 https://doi.org/10.1016/j.envint.2019.105281.

Wang, T., Liu, J., Yang, Y.H., Sui, Z.F., Zhang, Y.S., Wang, J.W., Pan, W.P., 2020b. Catalytic conversion of mercury over Ce doped Mn/SAPO-34 catalyst: Sulphur tolerance and SO_2/SO_3 conversion. J. Hazard. Mater. 381, 120986 https://doi.org/10.1016/j.jhazmat.2019.120986.

Wang, Z., Yang, Y.J., Liu, J., Liu, F., Yan, X.C., 2020c. Experimental and theoretical insights into the effect of syngas components on Hg^0 removal over $CoMn_2O_4$ sorbent. Ind. Eng. Chem. Res. 59, 8078–8085. https://doi.org/10.1021/acs.iecr.0c00251.

Wu, F.C., Tseng, R.L., Juang, R.S., 2009. Initial behavior of intraparticle diffusion model used in the description of adsorption kinetics. Chem. Eng. J. 153, 1–8. https://doi.org/10.1016/j.cej.2009.04.042.

Wu, X., Duan, Y.F., Li, N., Hu, P., Yao, T., Meng, J.L., Ren, S.J., Wei, H.Q., 2019. Regenerable Ce-Mn/TiO_2 catalytic sorbent for mercury removal with high resistance to SO_2. Energy Fuels 33, 8835–8842. https://doi.org/10.1021/acs.energyfuels.9b00978.

Xin, F., Xiao, R.H., Zhao, Y.C., Zhang, J.Y., 2022. Surface sulfidation modification of magnetospheres from fly ash for elemental mercury removal from coal combustion flue gas. Chem. Eng. J. 436, 135212.

Xu, H.M., Qu, Z., Zong, C.X., Quan, F.Q., Mei, J., Yan, N.Q., 2016. Catalytic oxidation and adsorption of Hg^0 over low-temperature NH_3-SCR $LaMnO_3$ perovskite oxide from flue gas. Appl. Catal. B: Environ. 186, 30–40. https://doi.org/10.1016/j.apcatb.2015.12.042.

Xu, H.M., Yan, N.Q., Qu, Z., Liu, W., Mei, J., Huang, W.J., Zhao, S.J., 2017. Gaseous heterogeneous catalytic reactions over Mn-based oxides for environmental applications: A critical review. Environ. Sci. Technol. 51, 8879–8892. https://doi.org/10.1021/acs.est.6b06079.

Xu, Y., Luo, G.Q., Zhou, M.L., Zhang, Q.Z., Li, Z.H., Zhang, S.B., 2021. Natural ferruginous manganese ore for efficient immobilization of elemental mercury from coal combustion flue gas. Fuel 283, 118946. https://doi.org/10.1016/j.fuel.2020.118946.

Xue, Y.Y., Guo, Y., Zhang, Z.G., Guo, Y.L., Wang, Y.Q., Lu, G.Z., 2008. The role of surface properties of activated carbon in the catalytic reduction of NO by carbon. Appl. Surf. Sci. 255, 2591–2595. https://doi.org/10.1016/j.apsusc.2008.07.167.

Yan, Z., Liu, L.L., Zhang, Y.L., Liang, J.P., Wang, J.P., Zhang, Z.T., Wang, X.D., 2013. Activated semi-coke in SO_2 removal from flue gas: Selection of activation methodology and desulfurization mechanism study. Energy Fuels 27, 3080–3089. https://doi.org/10.1021/ef400351a.

Yang, W., Wang, Z., Liu, Y., 2020a. Review on magnetic adsorbents for removal of elemental mercury from flue gas. Energy Fuels 34, 13473–13490 https:// doi.org/10.1021/acs.energyfuels.0c02931.

Yang, J.P., Xu, H., Chen, H., Meng, F.Y., Zu, H.X., Zhu, P.L., Yang, Z.Q., Li, M., Li, H.L., 2022a. Removal of flue gas mercury by porous carbons derived from one-pot carbonization and deactivation of wood sawdust in a molten salt medium. J. Hazard. Mater 424, 127336. https://doi.org/10.1016/j.jhazmat.2021.127336.

Yang, J.P., Zhao, Y.C., Ma, S.M., Zhu, B.B., Zhang, J.Y., Zheng, C.G., 2016. Mercury removal by magnetic biochar derived from simultaneous activation and magnetization of sawdust. Environ. Sci. Technol. 50, 12040–12047. https://doi.org/10.1021/acs.est.6b03743.

Yang, J.P., Zhao, Y.C., Liang, S.F., Zhang, S.B., Ma, S.M., Li, H.L., Zhang, J.Y., Zheng, C.G., 2018. Magnetic iron-manganese binary oxide supported on carbon nanofiber ($Fe_{3-x}Mn_xO_4$/CNF) for efficient removal of Hg^0 from coal combustion flue gas. Chem. Eng. J. 334, 216–224. https://doi.org/10.1016/j.cej.2017.10.004.

Yang, J.P., Zhu, P.L., Meng, F.Y., Guo, Q.J., He, T., Yang, Z.Q., Qu, W.Q., Li, H.L., 2022b. Charge distribution modulation and morphology controlling of copper selenide for an enhanced mercury adsorption activity in flue gas. Chem. Eng. J. 442, 136145 https://doi.org/10.1016/j.cej.2022.136145.

Yang, S.J., Guo, Y.F., Yan, N.Q., Wu, D.Q., He, H.P., Qu, Z., Jia, J.P., 2011. Elemental mercury capture from flue gas by magnetic Mn–Fe spinel: Effect of chemical heterogeneity. Ind. Eng. Chem. Res. 50, 9650–9656. https://doi.org/10.1021/ie2009873.

Yang, J.P., Li, Q., Zu, H.X., Yang, Z.Q., Qu, W.Q., Li, M., Li, H.L., 2020b. Surface-engineered sponge decorated with copper selenide for highly efficient gas-phase mercury immobilization. Environ. Sci. Technol. 54, 16195–16203. https://doi.org/10.1021/acs.est.0c04982.

Yang, Y.J., Liu, J., Wang, Z., Long, Y., Ding, J.Y., 2019. Interface reaction activity of recyclable and regenerable Cu-Mn spinel-type sorbent for Hg^0 capture from flue gas. Chem. Eng. J. 372, 697–707. https://doi.org/10.1016/j.cej.2019.04.177.

Zhang, B., Xu, P., Qiu, Y., Yu, Q., Ma, J.J., Wu, H., Luo, G.Q., Xu, M.H., Yao, H., 2015. Increasing oxygen functional groups of activated carbon with non-thermal plasma to enhance mercury removal efficiency for flue gases. Chem. Eng. J. 263, 1–8. https://doi.org/10.1016/j.cej.2014.10.090.

Zhang, H.C., Wang, T., Zhang, Y.S., Wang, J.W., Sun, B.M., Pan, W.P., 2020. A review on adsorbent/catalyst application for mercury removal in flue gas: Effect of sulphur oxides (SO_2, SO_3). J. Clean. Prod. 276, 124220 https://doi.org/10.1016/j.jclepro.2020.124220.

Zhang, H.L., Hu, W., Zhou, C.X., Liu, H.R., Yao, P., Wang, J.L., Chen, Y.Q., 2018. A new understanding of CeO_2-ZrO_2 catalysts calcinated at different temperatures: Reduction property and soot-O_2 reaction. Appl. Catal. A: Gene. 563, 204–215. https://doi.org/10.1016/j.apcata.2018.07.012.

Zhang, J., Li, C.T., Du, X.Y., Li, S.H., Huang, L., 2022. Recycle of waste activated coke as an efficient sorbent for Hg^0 removal from coal-fired flue gas. Fuel 324, 124645. https://doi.org/10.1016/j.fuel.2022.124645.

Zhang, X.P., Zhang, H., Zhu, H.D., Li, C.F., Zhang, N., Bao, J.J., He, G.H., 2019. Co_3O_4 nanorods with a great amount of oxygen vacancies for highly efficient Hg^0 oxidation from coal combustion flue gas. Energy Fuels 33, 6552–6561. https://doi.org/10.1021/acs.energyfuels.9b00765.

Zhao, Q., Zheng, Y.F., Song, C.F., Liu, Q.L., Ji, N., Ma, D.G., Lu, X.B., 2020. Novel monolithic catalysts derived from in-situ decoration of Co_3O_4 and hierarchical Co_3O_4@MnO_x on Ni foam for VOC oxidation. Appl. Catal. B: Environ. 265, 118552 https://doi.org/10.1016/j.apcatb.2019.118552.

Zhao, R., Jia, L., Yao, Y.X., Huo, R.P., Qiao, X.L., Fan, B.G., 2019. Study of the effect of adsorption temperature on elemental mercury removal performance of iron-based modified biochar. Energy Fuels 33, 11408–11419. https://doi.org/10.1021/acs.energyfuels.9b02468.

Zheng, Y.E., Li, K.Z., Wang, H., Wang, Y.H., Tian, D., Wei, Y.G., Zhu, X., Zeng, C.H., Luo, Y.M., 2016. Structure dependence and reaction mechanism of CO oxidation: A model study on macroporous CeO_2 and CeO_2-ZrO_2 catalysts. J. Catal. 344, 365–377. https://doi.org/10.1016/j.jcat.2016.10.008.

Zhou, J.H., Sui, Z.J., Zhu, J., Li, P., Chen, D., Dai, Y.C., Yuan, W.K., 2007. Characterization of surface oxygen complexes on carbon nanofibers by TPD, XPS and FT-IR. Carbon 45, 785–796. https://doi.org/10.1016/j.carbon.2006.11.019.

Zhou, Z.J., Liu, X.W., Xu, J., Cao, X.K.E., Zhu, X.B., 2019. Elemental mercury removal over a novel starch-modified MnO_x/bentonite composite. Fuel Process. Technol. 187, 16–20. https://doi.org/10.1016/j.fuproc.2019.01.006.

Zhou, Z.J., Liu, X.W., Li, C.P., Cao, X.K.E., Xu, M.H., 2020. Seawater-assisted synthesis of MnCe/zeolite-13X for removing elemental mercury from coal-fired flue gas. Fuel 262, 116605. https://doi.org/10.1016/j.fuel.2019.116605.

Zhu, Y.C., Hou, Y.Q., Wang, J.W., Guo, Y.P., Huang, Z.G., Han, X.J., 2019. Effect of SCR atmosphere on the removal of Hg^0 by a V_2O_5-CeO_2/AC catalyst at low temperature. Environ. Sci. Technol. 53, 5521–5527. https://doi.org/10.1021/acs.est.8b07122.